QUANTITATIVE MEASUREMENT AND FLOW VISUALIZATION OF WATER CAVITATION IN A CONVERGING-DIVERGING NOZZLE

by

AARON JAMES SCHMIDT

B.S., Kansas State University, 2012

A THESIS

submitted in partial fulfillment of the requirements for the degree

MASTER OF SCIENCE

Department of Mechanical and Nuclear Engineering
College of Engineering

KANSAS STATE UNIVERSITY
Manhattan, Kansas

2016

Approved by:

Co-Major Professor
Dr. B. Terry Beck

Approved by:

Co-Major Professor
Dr. M. H. Hosni

Copyright

Abstract

Cavitation is the change of a liquid to a two-phase mixture of liquid and vapor, similar to boiling. However, boiling generates a vapor by increasing the liquid temperature while cavitation generates vapor through a decrease in pressure. Both processes are endothermic, removing heat from the surroundings. Both the phase change and heat absorption associated with cavitation provide many engineering applications, including contributing to a new type of refrigeration cycle under development. Cavitation can occur at or below the vapor pressure; conditions that delay cavitation and allow for a metastable liquid are not well understood.

A converging-diverging nozzle was designed and fabricatedto create a low pressure region at the nozzle throat.The converging section of the nozzle increased the water velocity and decreased the pressure, according to Bernoulli's principle. A cavitation front was formed slightly past the nozzle throat. The cavitation location suggested that the water was metastable nearthe nozzle throat. Flow through the system was controlled by changing the nozzle inlet and outlet pressures. The flowrate of water was measured while the outlet pressure was lowered. The flowrate increased as the outlet pressure dropped until cavitation occurred. Once cavitation initiated, the flow became choked and remained constant and independent of the nozzle outlet pressure. High-speed imagery was used to visualize the flow throughout the nozzle and the formation and collapse of cavitation in the nozzle's diverging section. High-speed video taken from 1,000 to 35,000 frames per second captured the formation of the cavitation front and revealed regions of recirculating flow near the nozzle wall in the diverging section. Particle Image Velocimetry (PIV) was used to measure the velocity vector field throughout the nozzle to characterize flow patterns within the nozzle. PIV showed that the velocity profile in the converging section and throat region were nearly uniform at each axial position in the nozzle. In

the diverging section, PIV showed a transient, high-velocity central jet surrounded by large areas of recirculation and eddy formation. The single-phase experimental results, prior to cavitation onset, were supplemented by Computational Fluid Dynamics (CFD) simulations of the velocity distribution using Fluent software.

Table of Contents

List of Figures vii

List of Tables xii

Acknowledgements xiii

Dedication xiv

Chapter 1 - Introduction 1

1.1 Literature Review 3

1.1.1 Properties of Cavitating Flows 4

1.1.2 Limits of Cavitation 9

1.1.3 Simulation Considerations 10

1.2 Objectives 12

1.2.1 Effects of Pressure on Flowrate 13

1.2.2 High-Speed Visualization of Cavitation 13

1.2.3 Flow Field Visualization near Cavitation 13

1.2.4 Apply Commercial CFD Simulations to Support Measurements 14

Chapter 2 - Experimental Setup 15

2.1 Flow System 16

2.2 Test Section 17

2.3 Visualization Support Framework 18

2.4 PIV System 18

2.5 High-Speed Camera 20

Chapter 3 - Experimental Procedure 21

3.1 Operation of Flow System 21
3.2 High-Speed Digital Camera 22
3.3 PIV System 23
Chapter 4 - Experimental Results 26
4.1 Effects of Pressure on Flowrate 26
4.2 High-Speed Flow Visualization 32
4.3 Particle Image Velocimetry 45
Chapter 5 - CFD Simulations 53
5.1 Model Mesh 54
5.2 Low Velocity Model 56
5.3 High Velocity Model 60
5.4 Other Viscous Models 62
Chapter 6 - Conclusions and Recommendations 65
6.1 Summary and Conclusions 65
6.2 Recommendations for Future Work 68
References 69
Appendix A - PIV Equipment Specifications 70
Appendix B - High-Speed Digital Camera Specifications 72
Appendix C - Long-Distance Microscope and Lens Specifications 75
Appendix D - Software 76
Appendix E - Auxiliary Instrumentation and Uncertainty Specifications 77

List of Figures

Figure 1.1 Phase diagram of water. $p_v(T)$ is the saturated vapor pressure as a function of temperature [1] (© NATO STO). 1

Figure 1.2 Schematic of typical refrigeration cycle. 2

Figure 1.3 Examples of travelling bubble (A), sheet (B), vortex (C), and shear (D) cavitation [1] (© NATO STO). 4

Figure 1.4 Converging-diverging nozzle used by Rudolf [3]. 5

Figure 1.5 Partial cavitation (A), fully developed cavitation (B), and supercavitation (C) from [3]. Flow shown from left to right. 6

Figure 1.6 Flow through a rectangular jet with velocity profiles measured with laser Doppler velocimetry for no cavitation (a), developing cavitation (b) and (c), and supercavitation (d). Flow shown entering from top and exits to atmosphere [5]. 6

Figure 1.7 Effects of cavitation number and Reynolds number on cavitation regime (A). Effects of Reynolds number (B) and cavitation number (C) on normalized cavitation length [5]. 7

Figure 1.8 Bubbly shock in water with detailed view. Axial pressure distribution plotted for several back pressures [2]. 8

Figure 1.9 Equilibrium speed of sound c in two-phase mixture with (Franc and Michel [7]) and without (Wallis [6]) phase transition. Theoretical predictions from Franc and Michel compared with numerical data [4]. 9

Figure 1.10 Pressure and void fraction for different central-body nozzle concepts modelled using Fluent CFD software [10]. 11

Figure 1.11 Venturi contraction designed for studying CFD simulation accuracy for cavitating flow. Shown with schematic and model mesh [9]. 12

Figure 2.1 Flow system schematic. 15

Figure 2.2 Photo of Nozzle-1 (A), shown with schematic (B), and nozzle profile data (C). 17

Figure 2.3 Test section and camera schematic. 18

Figure 2.4 PIV setup schematic, shown from above. 19

Figure 2.5 High-speed camera setup with long distance microscope (LDM) attachment. 20

Figure 4.1 Pressure effects on flowrate for Nozzle-1. Inlet absolute pressure measured with liquid-filled pressure gauge and barometer. 27

Figure 4.2 Pressure effects on flowrate for Nozzle-2. Inlet absolute pressure of 104.0 ± 1 kPa measured with liquid-filled pressure gauge and barometer. 28

Figure 4.3 Comparison of vacuum chamber and test section absolute pressures for Nozzle-2. Test section inlet and outlet pressures measured with pressure transducers. Vacuum chamber pressure measured with dry pressure gauge and a barometer. 30

Figure 4.4 Measured pressure drop from test section inlet to outlet (nozzle pressure drop) and from test section outlet to downstream reservoir (downstream pressure drop) for Nozzle-2. 31

Figure 4.5 Nozzle-1 with scale in cm. Interior of nozzle outlined for emphasis. 32

Figure 4.6 High-speed video of bubble in converging section of Nozzle-1 with a vacuum chamber absolute pressure of 30 ± 2 kPa. 34

Figure 4.7 Cavitation onset in Nozzle-1 with a vacuum chamber absolute pressure of 27 ± 2 kPa. Time of images indicated in milliseconds 35

Figure 4.8 Cavitation onset in Nozzle-1 with a vacuum chamber absolute pressure of 9.6 ± 2 kPa. Time of images indicated in milliseconds 36

Figure 4.9 High-speed video of Nozzle-1 throat and diverging regions. Flow shown just before cavitation (A), with cavitation (B), and with cavitation and graduated grid (C). 37
Figure 4.10 Cavitation length shown at different vacuum chamber absolute pressures for Nozzle-1..... 39
Figure 4.11 Cavitation in Nozzle-1 with a vacuum chamber absolute pressure of 27 ± 2 kPa with degassed water (left) and tap water (right)..... 41
Figure 4.12 Normal cavitation in Nozzle-1 (A). Seed induced cavitation in Nozzle-1 (B). Detailed view of seed induced cavitation in Nozzle-1 (C). Vacuum chamber absolute pressure of 27 ± 2 kPa. Spherical 120 μm diameter glass seed particles..... 42
Figure 4.13 Recirculation of seed particle in Nozzle-1 with vacuum chamber absolute pressure of 49 ± 2 kPa. 43
Figure 4.14 Close view of recirculation of cavitation bubbles immediately downstream of throat in Nozzle-1..... 44
Figure 4.15 Nozzle-1 converging section averaged PIV. Velocity magnitude in m/s..... 46
Figure 4.16 Averaged PIV capture of Nozzle-1 throat section. Velocity magnitude in m/s. 47
Figure 4.17 PIV captures of throat and diverging section of Nozzle-1 with no cavitation. Velocity magnitude in m/s. Throat location indicated with dashed line..... 48
Figure 4.18 PIV captures of throat and diverging section of Nozzle-1 with cavitation. Velocity magnitude in m/s. Throat location indicated with dashed line. 49
Figure 4.19 Detailed view of reversed flow in diverging section of Nozzle-1. Color indicates Y-component of velocity (V) in m/s. Position of frame 2 indicated in frame 1. 50
Figure 4.20 PIV capture near wall of diverging section of Nozzle-1. Color indicates Y-component of velocity in m/s. Location indicated relative to throat. Grid size of 1.0 mm. 51

Figure 4.21 PIV captures near wall in Nozzle-1. Location indicated in Figure 4.20. Color indicates Y-component of velocity in m/s. 52
Figure 5.1 CFD model mesh (left) shown with corresponding real nozzle (right) in vertical orientation. Mesh zones shown in separate colors. 53
Figure 5.2 CFD model mesh detail of Nozzle-1's converging, throat, and diverging sections. Converging and diverging sections shown on same scale, throat section enlarged. Model contained 617,000 elements. 54
Figure 5.3 CFD k-ε model velocity magnitude (left) and vertical velocity (right) contour plots with uniform inlet velocity of 0.2 m/s. Velocities plotted in m/s. 56
Figure 5.4 Inlet section velocity profile for inlet velocities of 0.2 m/s (bottom) and 0.6 m/s (top). 58
Figure 5.5 CFD normalized axial velocity vs normalized radial position for several positions at and downstream of nozzle throat for inlet velocity of 0.2 m/s. 58
Figure 5.6 CFD model static pressure (kPa) contour plot for inlet velocity of 0.2 m/s. 59
Figure 5.7 CFD k-ε model velocity magnitude (left) and vertical velocity (right) contour plots with uniform inlet velocity of 0.6 m/s. Velocities plotted in m/s. 60
Figure 5.8 CFD normalized axial velocity vs normalized radial position for several positions at and downstream of nozzle throat for inlet velocity of 0.6 m/s. 61
Figure 5.9 CFD model static pressure (kPa) contour plot for inlet velocity of 0.6 m/s. 62
Figure 5.10 CFD detached eddy simulation (DES) model velocity magnitude (m/s) contour plot with uniform inlet velocity of 0.5 m/s. 63
Figure A.1 PIV camera shown with 60 mm lens. 70
Figure A.2 Nd:YAG laser. 71

Figure A.3 PIV synchronizer. 71

Figure B.1 High-speed digital camera. Shown with 60 mm lens. 74

Figure C.1 Long-distance microscope. 75

Figure E.1 Dry Ashcroft (left) and liquid-filled Wika (right) pressure gauges. 79

Figure E.2 Barometer used for absolute pressure calibration, shown on side. Top of barometer shown in left side of photo. 80

Figure E.3 Omegadyne (top) and Viatran (bottom) pressure transducers. 81

Figure E.4 Rotameter with attached liquid-filled pressure gauge..... 81

List of Tables

Table B.1 High-speed digital camera model specifications..... 72

Table B.2 High-speed digital camera framerate and recording durations. Recording times (Rec. Times) are in seconds..... 73

Table C.1 Long-distance microscope lens working distance (WD), magnification (MAG), and field of view (FOV). 75

Acknowledgements

I would like to extend my sincere thanks and gratitude to Dr. Terry Beck and Dr. Mo Hosni. Dr. Beck always brought a multitude of ideas to every meeting, which always came with a story, or two. I am grateful for the numerous teaching opportunities and support he provided me, which helped me grow and develop as an engineer and person. Dr. Hosni's support was paramount to the completion of this thesis. His not so gentle encouragement was invaluable, and very much appreciated. I would also like to thank the KSU scientific glassblower, Jim Hodgson, for creating the beautiful glass nozzles on which our research was centered. I also thank Dr. Steve Eckels for his time on my committee and the numerous classes he has taught to me.

Finally, I must extend a special thanks to my former undergraduate research assistant, Alan Duong. Alan's curiosity and drive made lab work an absolute joy. His passion for science and engineering took him to the Universityof Notre Dame for graduate studies, but his effect has been long-lasting.

Dedication

I dedicate my thesis to my family. Each of you have supported and encouraged me through this journey. I hope I can provide the same loving environment that all my parents have created for me. My stepparents have grown into truly wonderful friends, who I dearly love. Trevor and Dalton, I am very proud to call you brother. Dalton, thank you especially for your support over the last year. Jen, I admire your passion; your encouragement and patience have provided me strength. Again, I thank my family, those who are with us, and those who join in spirit.

Chapter 1 - Introduction

Water remains liquid at standard atmospheric pressure and room temperature (21° C). If the pressure is held constant while the temperature is increased, water will produce vapor through boiling, as shown in Figure 1.1. If the temperature is held constant and the pressure sufficiently decreased, water will also form vapor; this process is typically referred to as cavitation. In both cases of vapor production, an absolute pressure below the saturated vaporpressure of water must be achieved. The saturated vapor pressure is a function of the fluid temperature. In the process of cavitation, the reduction below the vapor pressure is achieved through a reduction in the fluid pressure; while in boiling, the vapor pressure is increased due to the temperature rise in the fluid.

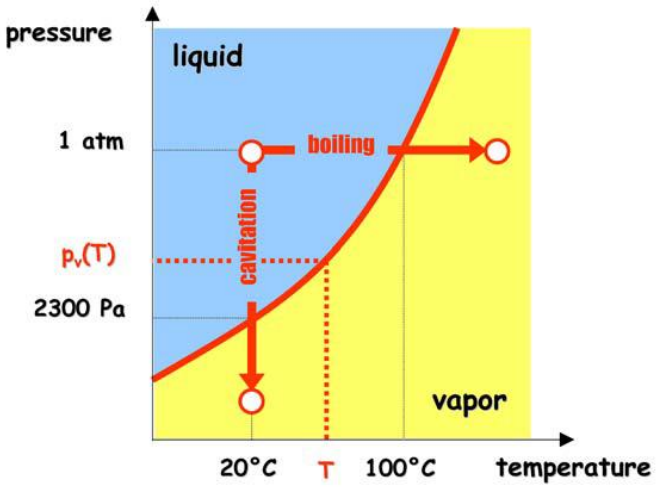

Figure 1.1 Phase diagram of water. $p_v(T)$ is the saturated vapor pressure as a function of temperature [1] (© NATO STO).

Cavitation in engineering applications such as pumps usually occurs due to the pressure depression accompanied by increased fluid velocity, as dictated by Bernoulli's principle. In such applications as pumps, the formation of cavitation is also accompanied by the collapse of cavitation bubbles when the fluid pressure rises above the vapor pressure. This cavitation

collapse can impart significant energy to solid surfaces and erode pump components. The formation of vapor also introduces a compressible fluid into the flow system, which can limit flowrates in components designed for incompressible liquid flow. For these reasons, if not properly understood and designed for, cavitation can cause significant reduction in performance of engineering components.

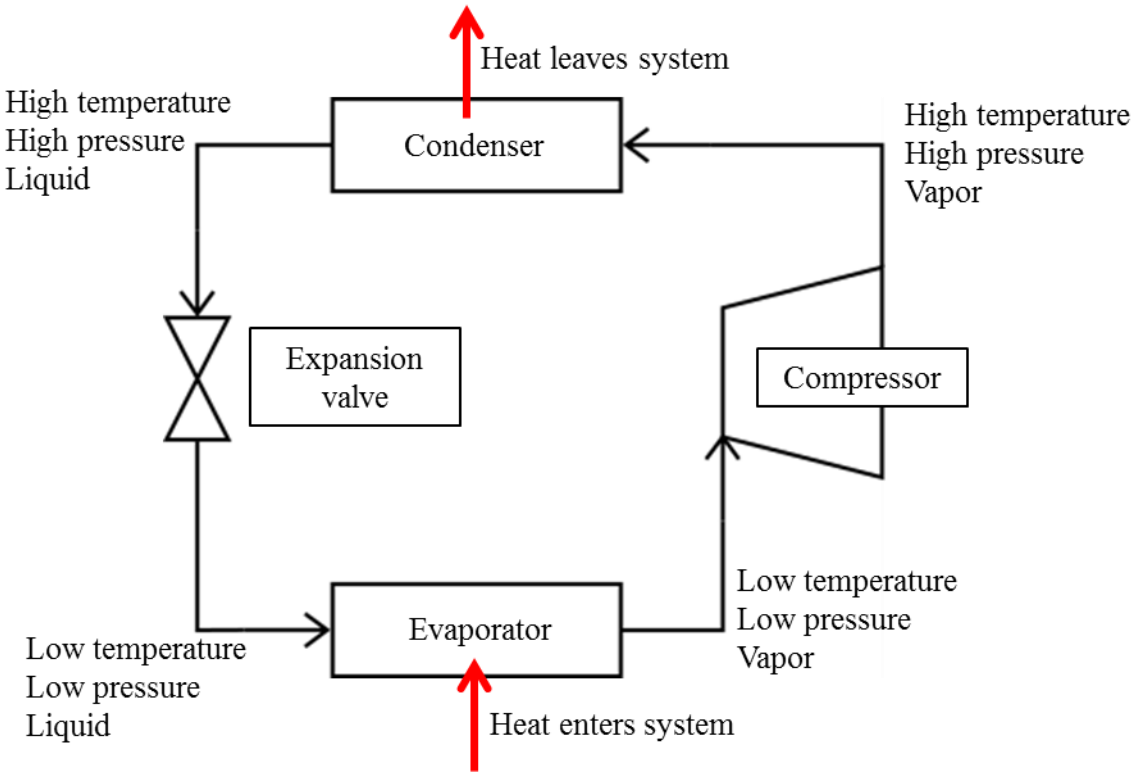

Figure 1.2 Schematic of typical refrigeration cycle.

The phase change of cavitation can also be exploited for potential performance gains in engineering applications such as refrigeration. Figure 1.2 shows a typical vapor-compression refrigeration cycle. The working fluid is introduced as a high temperature and pressure vapor and pumped through the condenser. The condenser removes heat from the working fluid, allowing the working fluid to condense into liquid. An expansion valve controls the flow to supply low-pressure liquid at the valve exit. The low temperature and pressure liquid enters the

evaporator and absorbs heat, facilitating evaporation. The vapor produced in the evaporator is then returned to the compressor.

The phase changes of the working fluid in the refrigeration cycle facilitate the transportation of heat in and out of the system. Condensation is an exothermic process, providing heat to the fluid's surroundings, while evaporation is an endothermic process, removing heat from the surroundings. The traditional refrigeration cycle employs an expansion valve and evaporator to take the working fluid from high temperature and pressure liquid to a low temperature and pressure vapor. An alternate refrigeration cycle could utilize a cavitation device to produce vapor and absorb heat from the fluid's surroundings, replacing the evaporator.

1.1 Literature Review

Publications concerning the formation of cavitation, including [1], [2], [3], and [4], classify at least four distinct cavitation forms. Travelling bubble cavitation, identified as A in Figure 1.3, forms from nucleation sites in the flow, typically microbubbles. These nucleation sites are nearly invisible in the liquid bulk until low-pressure regions below the vapor pressure drive their expansion into macroscopic bubbles. Attached, or sheet, cavitation typically forms large, steady voids near the onset of cavitation and an unsteady sheading of the cavitation voids near cavitation collapse. Sheet cavitation, shown in Figure 1.3, is typically attached to a surface in a steady fashion. The trailing edge of sheet cavitation sheds vapor structures in a periodic fashion. A 3D hydrofoil, shown in Figure 1.3, creates a vortex at the hydrofoil's tip. The pressure difference between the pressure and suction sides generates a secondary flow around the hydrofoil's tip. The core of the generated vortex is the lowest point of pressure due to centrifugal forces and is therefore the preferred location of cavitation formation. Similar to vortex cavitation, shear cavitation is generated in regions of high velocity gradients. The wake

produced by flow around a blunt shape, such as shown in Figure 1.3, can generate shear cavitation where the wake meets the bulk flow. Shear cavitation may also form around flow structures such as submerged jets [1].

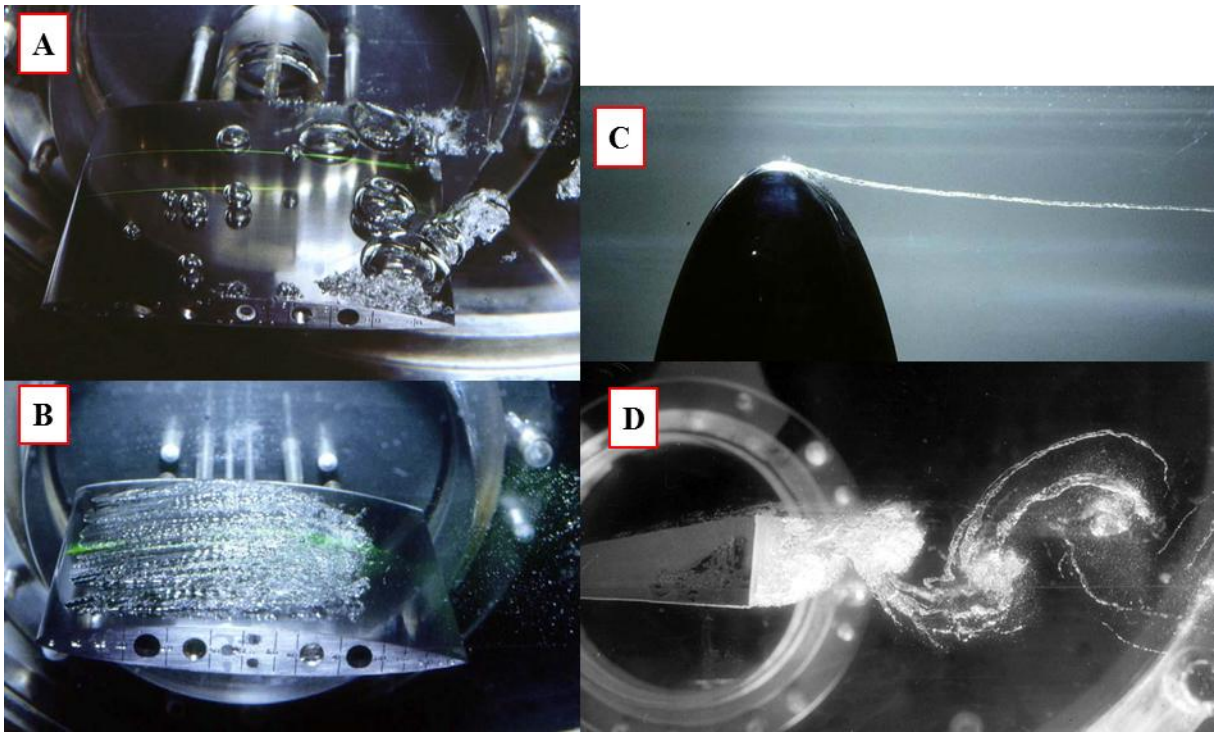

Figure 1.3 Examples of travelling bubble (A), sheet (B), vortex (C), and shear (D) cavitation [1] (© NATO STO).

1.1.1 Properties of Cavitating Flows

As previously discussed, the static pressure of a fluid must decrease as fluid velocity increases, in accordance with Bernoulli's principle. As the static pressure drops below the vapor saturation pressure, p_v, cavitation can occur. A non-dimensional cavitation parameter that relates the pressure and velocity information to the formation of cavitation is often considered. Franc [1] describes such a cavitation number in (1) where the reference pressure and velocity depend on the flow configuration.

$$\sigma_v = \frac{p_{ref} - p_v}{\frac{1}{2}\rho {V_{ref}}^2} \tag{1}$$

These values are usually the velocity and pressure of the bulk flow, far from any obstruction, for external flows. Rudolf [3]defined a cavitation number based on the outlet pressure and throat velocity of water flow through a converging-diverging nozzle in order to develop a loss coefficient for the different cavitation regimes. Regardless of its definition, the cavitation number describes the phase behavior of the fluid flow. For flows with high cavitation numbers, the flow is free of cavitation. The cavitation number decreases by corresponding decreases in pressure or increases in velocity until a critical value is reached. This critical value is the point of incipient cavitation. Developed cavitation corresponded to cavitation numbers smaller than the critical value. When the critical value is approached from developed cavitation, a cavitation number higher than the critical value is required before cavitation disappears[1].

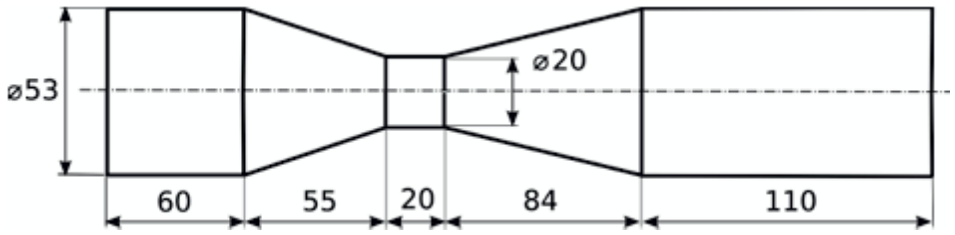

Figure 1.4 Converging-diverging nozzle used by Rudolf [3].

Rudolf [3] constructed a converging-diverging nozzle, shown in Figure 1.4, with sharp edges to show the relative locations of cavitation flow patterns. The flow circuit developed by Rudolf [3] was able to exhibit several cavitation patterns, shown in Figure 1.5. Rudolf was able to visualize regimes of partial cavitation (developing cavitation), fully developed cavitation, and supercavitation. Rudolf [3], Schaber [4], and Sou [5]all described supercavitation, a cavitation regime with a lower cavitation number than developed cavitation. Flow with extended pure vapor regions characterized supercavitation. Sharp interfaces separate the liquid and vapor phases of supercavitation. Rudolf [3] confirmed that supercavitation had created saturated water

vapor with direct pressure measurements taken at the nozzle's exit. This saturated vapor violently condensed in the downstream reservoir.

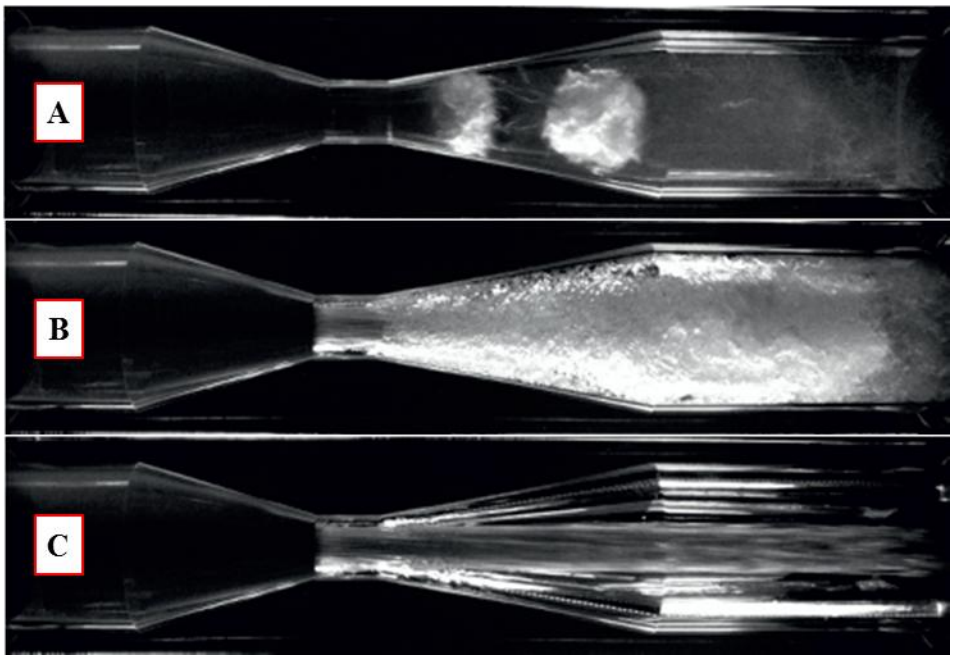

Figure 1.5Partial cavitation (A), fully developed cavitation (B), and supercavitation (C) from [3]. Flow shown from left to right.

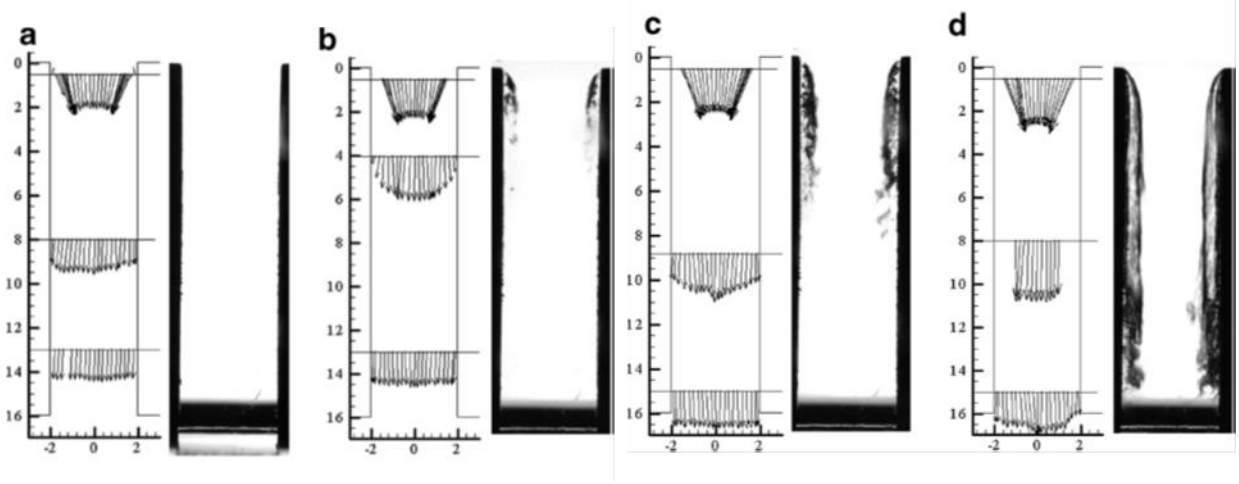

Figure 1.6 Flow through a rectangular jet with velocity profiles measured with laser Doppler velocimetry for no cavitation (a), developing cavitation (b) and (c), and supercavitation (d). Flow shown entering from top and exits to atmosphere [5].

Sou [5]employed laser Doppler velocimetry (LDV) and manual visual measurements to study the effects of Reynolds number and cavitation number on flow through a 2D rectangular

nozzle, shown in Figure 1.6. LDV measurements from the distinct cavitation regimes show how cavitation shapes the liquid flow through the nozzle.Figure 1.7 shows the cavitation regime (no cavitation, developing cavitation, and supercavitation) was mostly insensitive to changes in Reynolds number as long as the cavitation number was conserved. Likewise, the normalized cavitation length was strongly dependent on the cavitation number, not the Reynolds number.

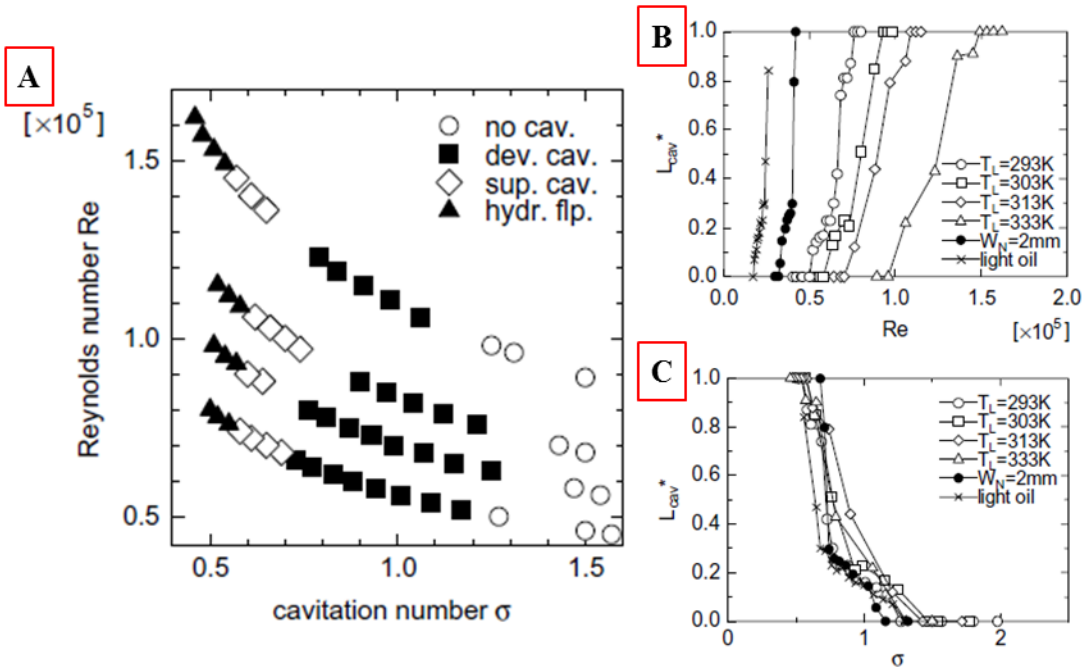

Figure 1.7 Effects of cavitation number and Reynolds number on cavitation regime (A). Effects of Reynolds number (B) and cavitation number (C) on normalized cavitation length [5].

The development of cavitation was a limiting factor for operation of all hydraulic machines and devices. The development of cavitation in these systems formed a two-phase compressible fluid which at the least substantially increased hydraulic losses and at worst damaged the flow system due to the high energy imparted during cavitation collapse [2] [3] [4]. Choked flow from the resultingtwo-phase mixture occurred with a sufficient pressure ratio, forming bubbly shocks shown in Figure 1.8. The axial pressure distribution shown in Figure 1.8 highlights the sudden rise in pressure where bubbly shocks occurred. This choked flow behavior

mimics choked flow in a single-phase, compressible gas with a sufficient pressure ratio to reach a sonic condition at the flow's constriction.

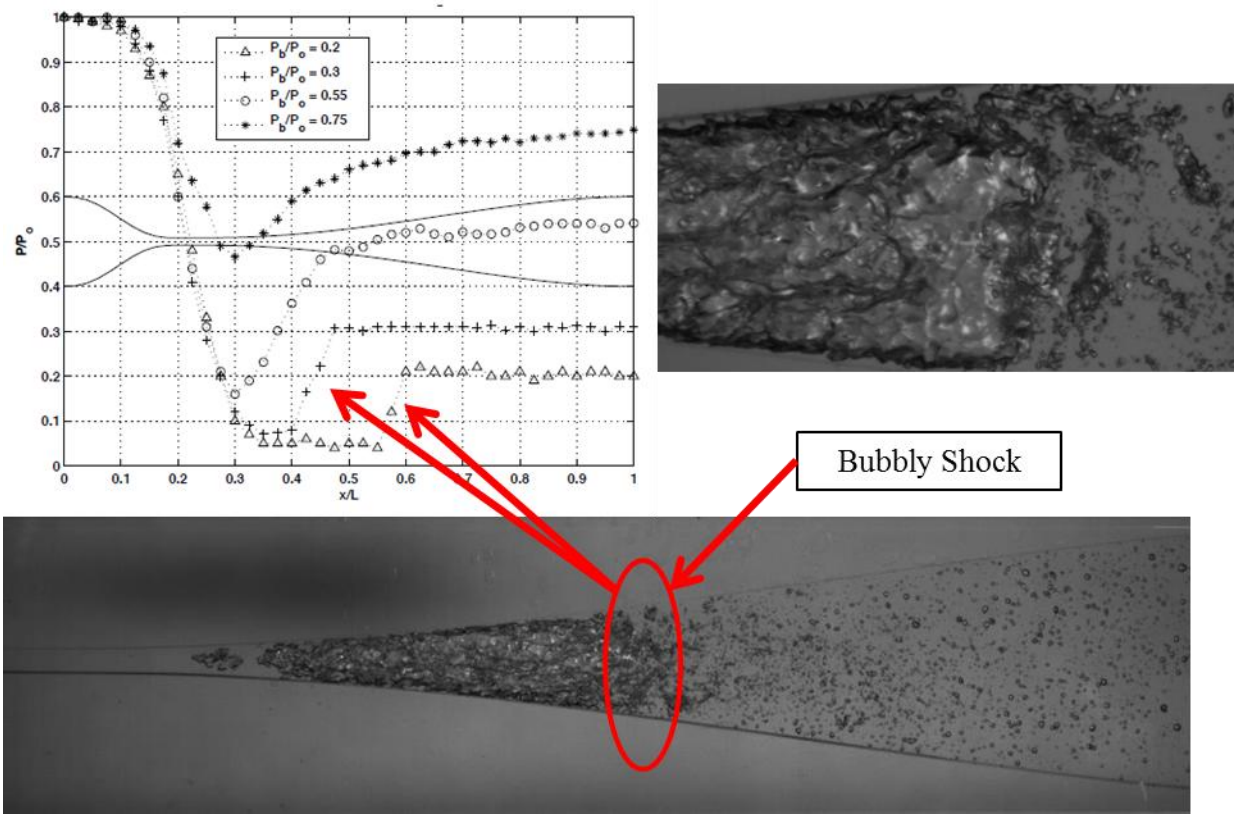

Figure 1.8 Bubbly shock in water with detailed view. Axial pressure distribution plotted for several back pressures [2].

Schaber [4] discussed the equilibrium speed of sound for a two-phase mixture and highlighted the importance of considering the phase transition associated with cavitating flow. Wallis [6] predicts a minimum equilibrium speed of sound of 4.3 m/s in a two-phase water mixture with a 0.5 vapor void fraction. This represented a several orders of magnitude reduction in the speed of sound from the pure liquid phase. Franc and Michel [7] added an additional term to Wallis's result, accounting for the phase transition, shown in Figure 1.9, which further reduced the predicted equilibrium speed of sound for low void fractions. This predicted a minimum speed of sound of 0.136 m/s at a vapor void fraction of 0.5.

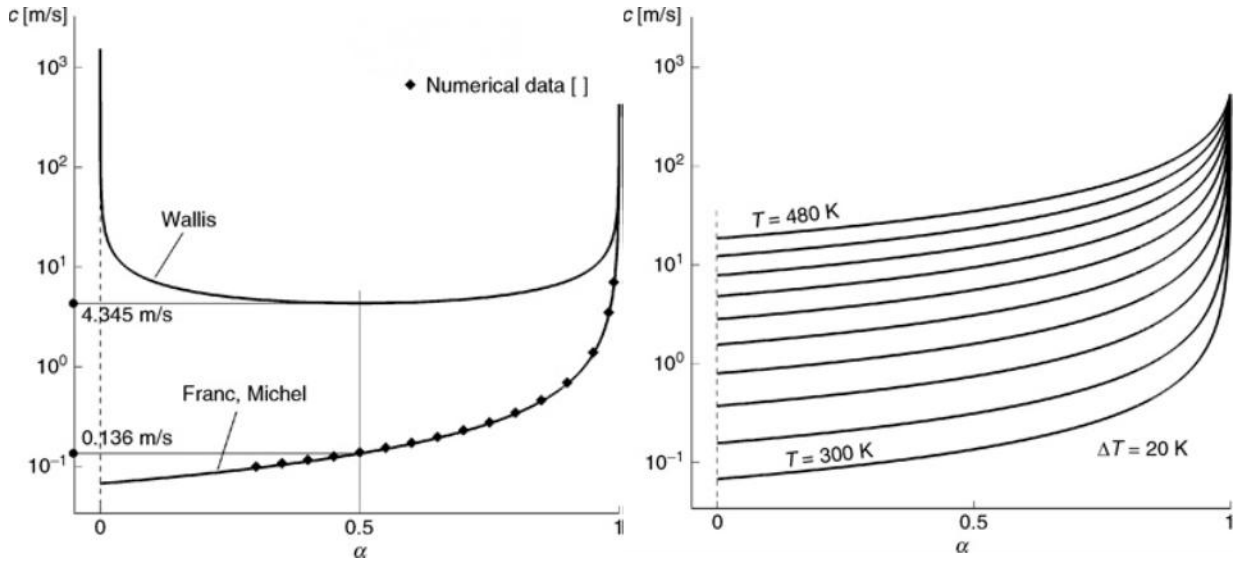

Figure 1.9 Equilibrium speed of sound c in two-phase mixture with (Franc and Michel[7]) and without (Wallis[6]) phase transition. Theoretical predictions from Franc and Michel compared with numerical data [4].

$$\Delta T^* = \frac{\rho_v L}{\rho_l c_{pl}} \tag{2}$$

Franc [1] described a temperature drop in cavitating flow in (2) which depends heavily on the ratio of liquid to vapor density and heat capacity of the fluid. For fluids like water, the temperature drop was on the order of 0.01 K. This temperature parameter becomes significant for cryogenic fluids such as liquid hydrogen or Refrigerant 114.

1.1.2 Limits of Cavitation

The high surface tension of water allows specialized flow structures, such as the capillaries that carry water from a tree's roots to its leaves, to create metastable, negative pressures. Caupin [8] reviewed several studies that hoped to reach the large negative pressures that are theoretically possible because of the properties of water. Acoustic-based studies have observed cavitation pressures of -30 MPa. Another study used cooled a micrometer sized water droplet trapped in a quartz crystal to reach a cavitation pressure of -140 MPa [8]. These studies exploited the surface tension, which was the dominant force at these microscopic scales.

1.1.3 Simulation Considerations

The simulation of cavitating flows requires several considerations determined by fluid and flow characteristics. For example, Schaber [4]demonstrated that the temperature effects of cavitation could be neglected in water. Simulations must model the speed of sound properly, such as is detailed in [7]. Simulation models of cavitation are formed in one of two ways. The first method, interface fitting, spits the flow into regions of liquid and vapor flow with a clearly defined interface. Secondly, continuum modelling treats the flow as two-phase with an averaged mixture density [9]. Interface methods were limited to flows where cavitation was limited to a clearly defined region. The continuum model more accurately included the physics of cavitation. Standard eddy-viscosity models suffered from over-production of eddy-viscosity, reducing the development of unsteadiness. Eddy-viscosity models have arbitrary limited turbulence production to obtain unsteady flow characteristics such as structure shedding and re-entrant jet formation[9].

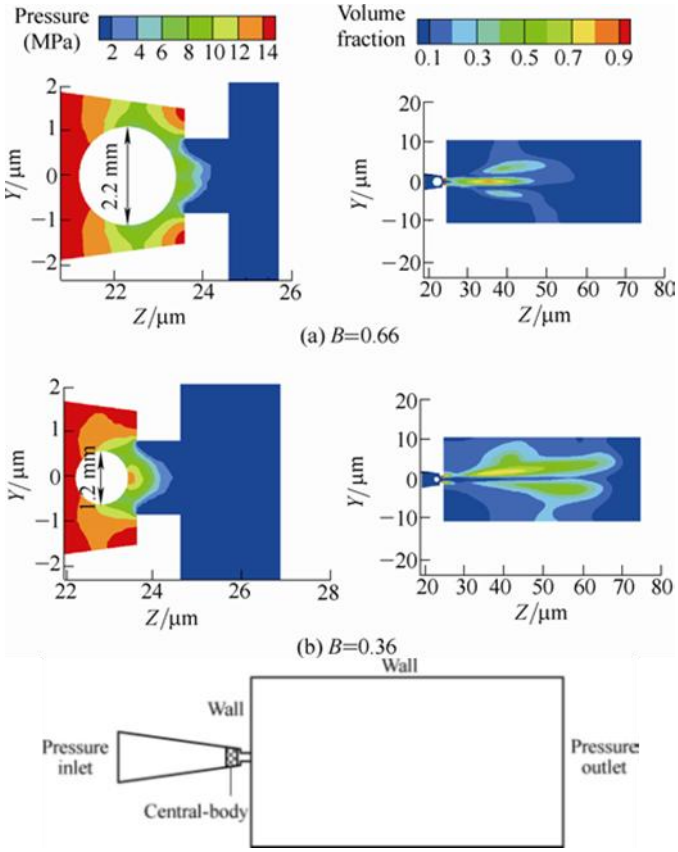

Figure 1.10Pressure and void fraction for different central-body nozzle concepts modelled using Fluent CFD software [10].

Commercially available software, such as Fluent, is typically used for computational fluid dynamics (CFD) modelling. This software allows for precise control over all aspects of modelling. Yang [10] used Fluent to model cavitation of a submerged jet generated by a novel central-body nozzle, shown in Figure 1.10. The simulation used a RNG k-epsilon turbulence model and full cavitation model. Another model created by Goncalves [9], shown in Figure 1.11, used a Venturi to generate sheet cavitation. Goncalves compared results from experiments with several CFD models, varying the equation of state and turbulence models for both steady and transient computations. Goncalves found good agreement with experimental results when a sufficiently small time steps were used. The times steps need to be small enough to stably simulate all physics applied in the model

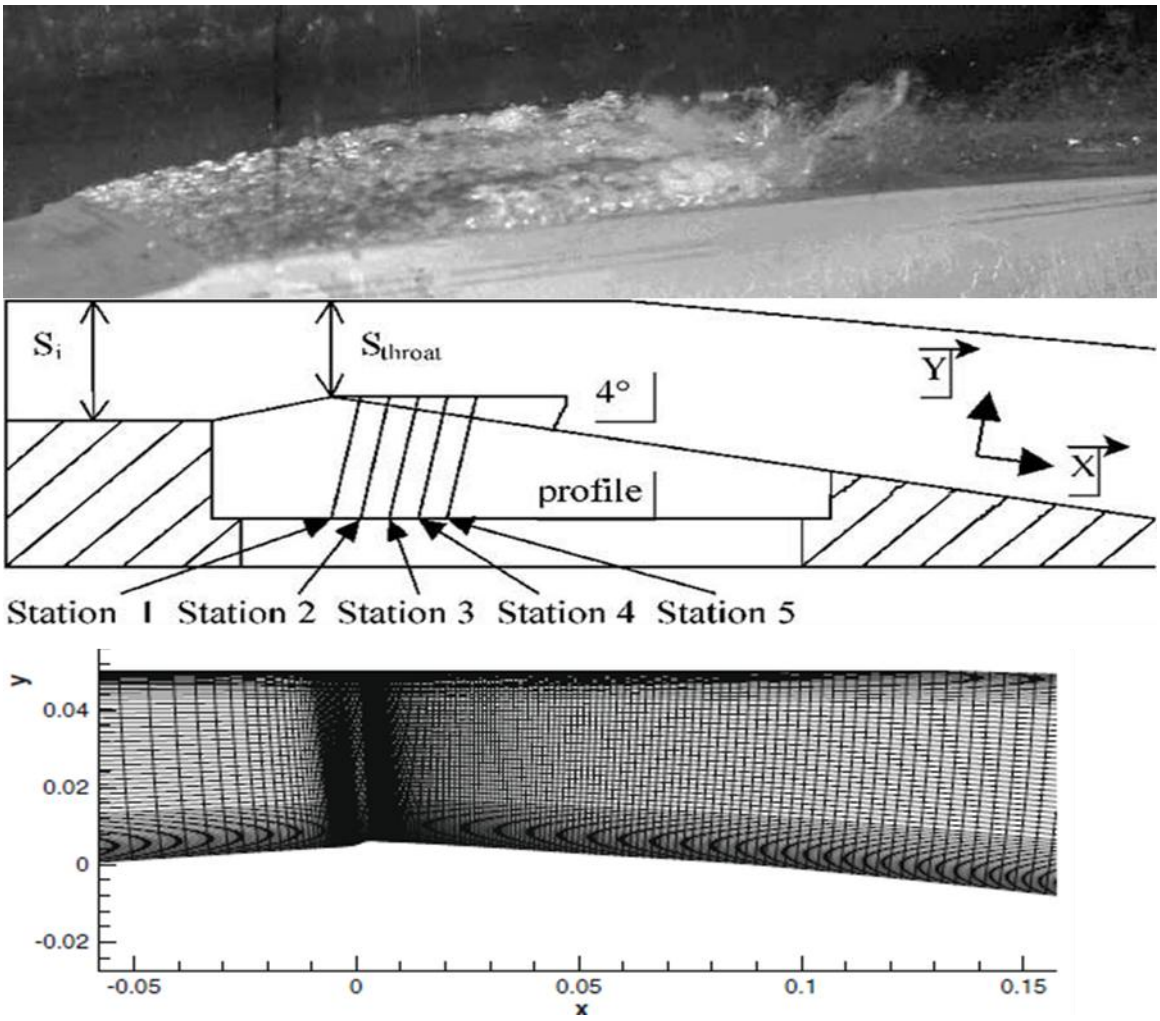

Figure 1.11Venturi contraction designed for studying CFD simulation accuracy for cavitating flow. Shown with schematic and model mesh [9].

1.2 Objectives

The work presented here aimed to study the formation and properties of cavitation produced by water flow through a converging-diverging nozzle, also known as a de Laval nozzle. Two cavitation-producing nozzles were studied. The nozzles were constructed from optically clear glass, permitting visualization of internal cavitation and fluid flow. An upstream and downstream reservoir produced a differential pressure, driving water flow through the test section. Sufficient water flow produce cavitation in the high velocity, low-pressure test section.

1.2.1 Effects of Pressure on Flowrate

A flow system was constructed to control the inlet and outlet pressures of a test section, in order to control the production of cavitating water flow within the test section. The effects of changing test section inlet and outlet pressures on the volumetric flowrate through the test section were studied. Both low flow without cavitating flow and high flow cavitating flow were studied. Studying these relationships allowed precise control of cavitating flow in the test section.

1.2.2 High-Speed Visualization of Cavitation

A high-speed digital camera was used to visualize flow structures within the test section. The overall cavitating flow was visualized to identify flow structures for a variety of test section conditions. The effects of the tests section inlet and outlet conditions were visualized to measure the cavitation length for each condition. The regions near incipient cavitation were closely visualized to investigate flow patterns near the cavitation front. Flow visualization near incipient cavitation was used to determine the location of the cavitation front in relation to regions of boundary layer separation. High-speed visualization of tracer particles provided flow structure information in these regions without the aid of cavitating flow.

1.2.3 Flow Field Visualization near Cavitation

Quantitative measurements of the velocity field were conducted using Particle Image Velocimetry (PIV). Measurements were made in several specific locations within the nozzle as well within the overall nozzle. Detailed measurements taken in the nozzle inlet region examined the velocity field in the nozzle inlet and converging sections. Additional PIV measurements investigated the velocity field of the nozzle's diverging section. Small field of view PIV measurements in the diverging section examined the detailed flow structures near the cavitation

front location. Most PIV measurements made of single-phase flow, just before incipient cavitation; however, some PIV measurements were taken near areas of cavitating flow where seeding and laser light were sufficient to capture quality velocity fields.

1.2.4 Apply Commercial CFD Simulations to Support Measurements

Commercially available computation fluid dynamics (CFD) software, Fluent, was used to model the nozzle geometry and flow conditions which were also measured by PIV. The velocity vector field obtained from the CFD model was compared to experimentally gathered PIV measurements to evaluate the validity of the CFD model and support the PIV measurements. CFD pressure distribution was also examined were pressure information was not gathered experimentally. Several viscosity models were investigated to determine the most cost effective model for the nozzle.

Chapter 2 - Experimental Setup

The experimental setup was developed to supply the required inlet and outlet conditions for the test section, which consisted of a converging-diverging glass nozzle. Figure 2.1shows the components assembled to drive the water flow through nozzle the test section. The test section inlet pressure, label 3 in Figure 2.1, was controlled by the evaluation of the upstream reservoir, which was open to atmospheric pressure and supplied water to the system. The vacuum pump created the low-pressure conditions inside the downstream reservoir to control the test section outlet pressure, label 4 in Figure 2.1. Several valves were used to control the flow from the upstream reservoir, through the test section, and to the downstream reservoir. Controlling the test section inlet and outlet conditions was necessary in order to gather the desired flow visualizations and Particle Image Velocimetry (PIV) data.

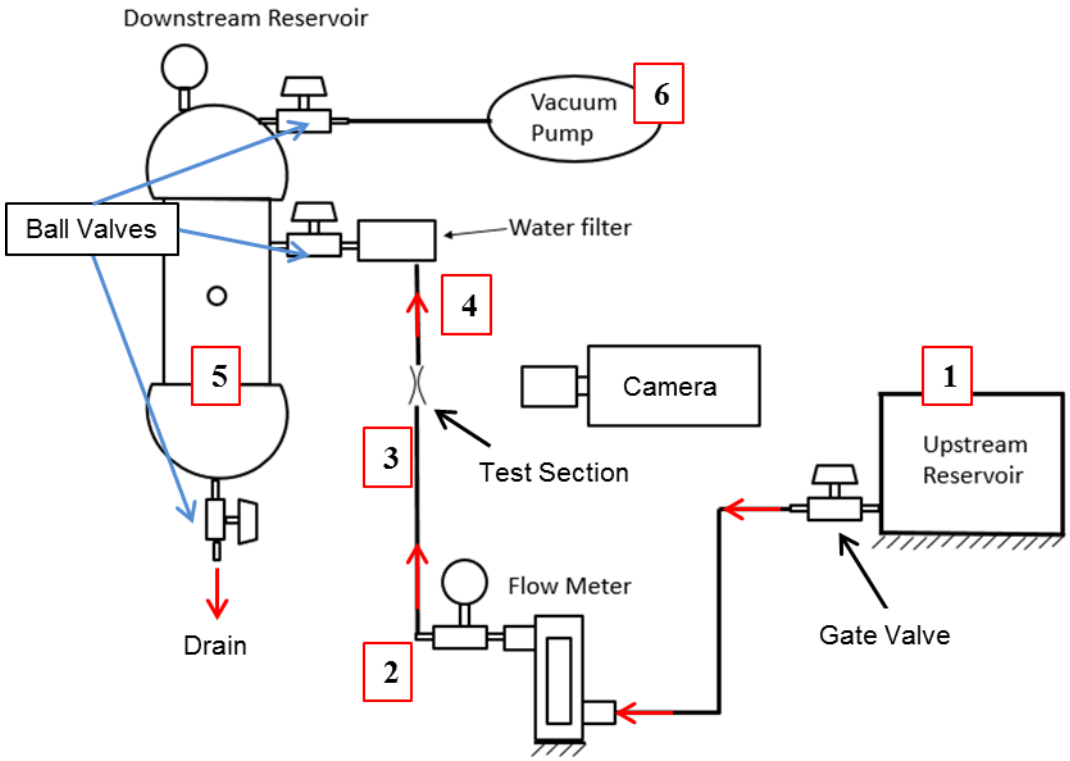

Figure 2.1 Flow system schematic.

2.1 Flow System

The flow began in the upstream reservoir open to atmospheric pressure, label 1 in Figure 2.1. A gate valve controlled flow from the upstream reservoir. The elevation of the upstream reservoir was used to control the test section inlet pressure. Resting the upstream reservoir on the lab floor provided a negative gauge pressure at the test section inlet, label 3 in Figure 2.1, while raising the upstream reservoir to two meters above the floor provided a positive gauge pressure at the test section inlet. Water was driven from the upstream reservoir through a rotameter and brass tee fitting, label 2 in Figure 2.1, to the test section inlet. The rotameter enabled direct volumetric flowrate measurement. A brass tee fitting housed a pressure gauge which provided pressure data at the exit of the rotameter. The water exited the test section outlet, label 4, traveled through a ball valve, then a water filter, and was then deposited in the downstream reservoir, label 5 in Figure 2.1. Air was evacuated from the downstream reservoir to provide a negative gauge pressure to drive water flow in the correct direction through the test section. The vacuum pump, label 6 in Figure 2.1, was connected to the downstream reservoir with a ball valve to remove air from the downstream reservoir. A ball valve on the bottom of the downstream reservoir allowed for draining of the downstream reservoir.

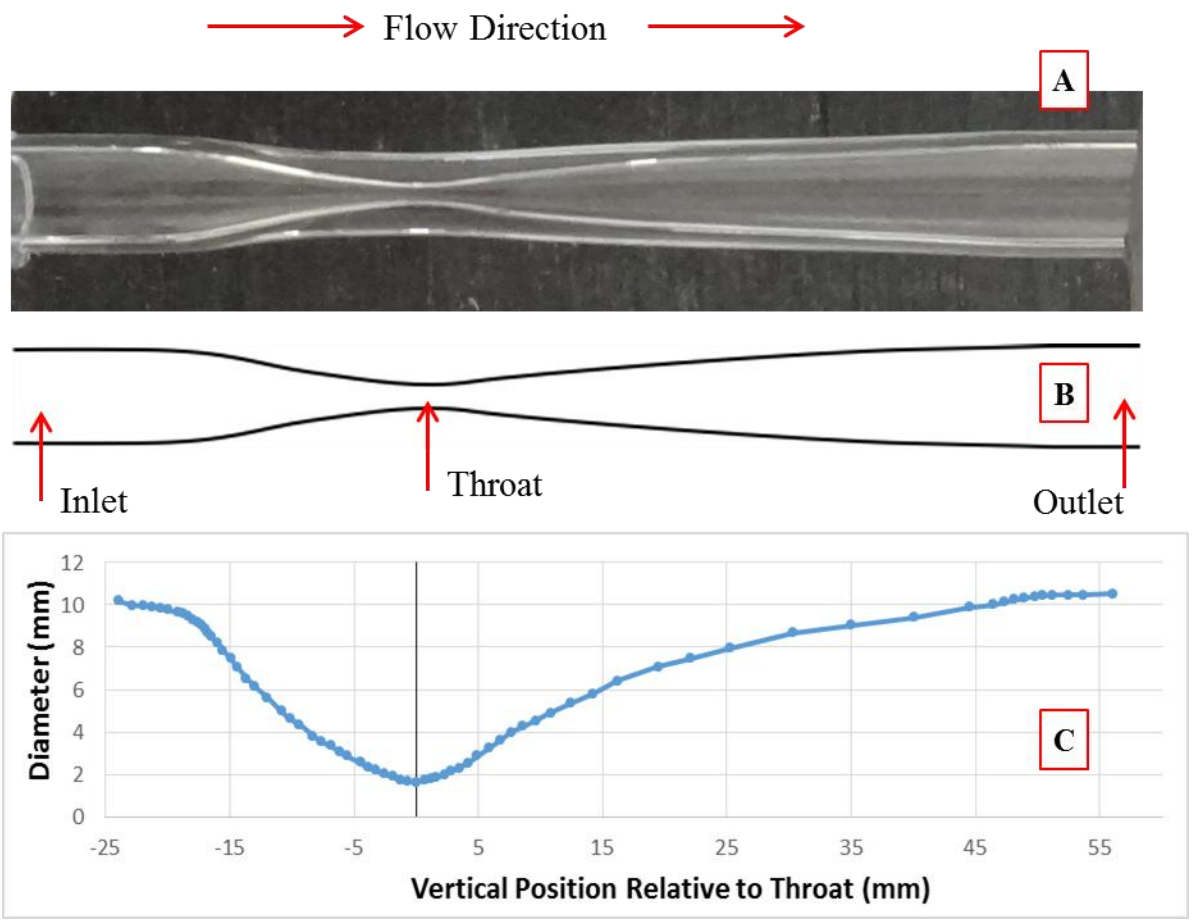

Figure 2.2Photo of Nozzle-1 (A), shown with schematic (B), and nozzle profile data (C).

2.2 Test Section

The test section used for experimentation, shown in Figure 2.1, housed the converging-diverging glass nozzle. Figure 2.2 shows Nozzle-1 (A) and the nozzle's diameter at each axial position relative to the minimum diameter at the nozzle throat (B). Two different nozzles were used for experimentation and each was formed by hand[1]. Nozzle 1, shown on its side in Figure 2.2, was formed with a short converging section reducing down to 1.62 mm at its throat. A long diverging section was formed after Nozzle-1's throat.

[1]Nozzles were formed from Pyrex glass tubing by Jim Hodgson, Senior Scientific Glassblower in the Department of Chemistry at Kansas State University.

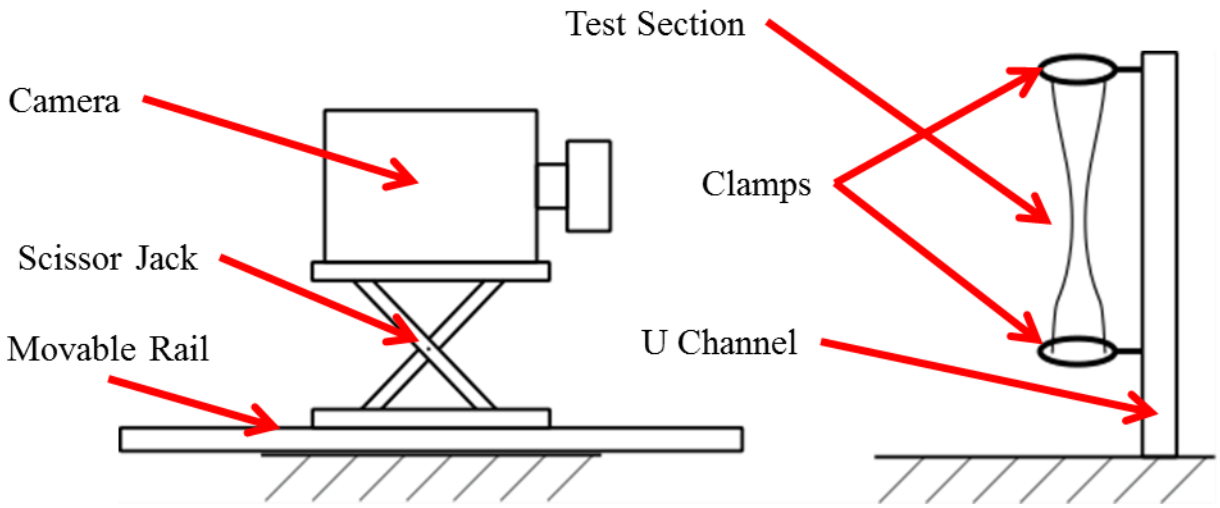

Figure 2.3Test section and camera schematic.

2.3 Visualization Support Framework

Employing high-speed imagery or Particle Image Velocimetry (PIV) for detailed flow visualization required stable supports for the test section, cameras, and other optical apparatus. A modified U-Channel support held the test section in a consistent vertical position, as shown in Figure 2.3. A scissor jack controlled the vertical position of the camerastage while a movable rail controlled the distance between the camera (high-speed or PIV) and the test section. Another scissor jack combined with a screw-driven linear stage allowed for precision lateral and vertical alignment of the PIV laser. The optical setup was assembled on an optics table, which provided the necessary support and alignment for the test section and optical setup.

2.4 PIV System

PIV provided velocity field data from the test section. Figure 2.4 shows the PIV system configuration. The Insight 4G software running on a desktop computer controlled the operation of the PIV system. The timing profile set in the software was communicated to the timing controller, also known as the synchronizer. The synchronizer triggered both the lasers and the PIV camera. The YAG laser required a signal for its flashlamp and Q-switch delay. The Q-

switch delay determined the intensity of laser light discharged for each laser pulse. The synchronizer coordinated the two YAG lasers to produce the time between laser pulses (delta T) prescribed by the timing setup in the software. Each laser pulse traveled through light arm, which guided the pulse to the light sheet optics. The light sheet optics formed each laser pulse into a narrow sheet. A screw adjustment on the light sheet optics allowed for adjustment of the focal distance of the light sheet waist. The light sheet illuminated seed particles traveling through the test section. Appendix A details the specific PIV equipment used.

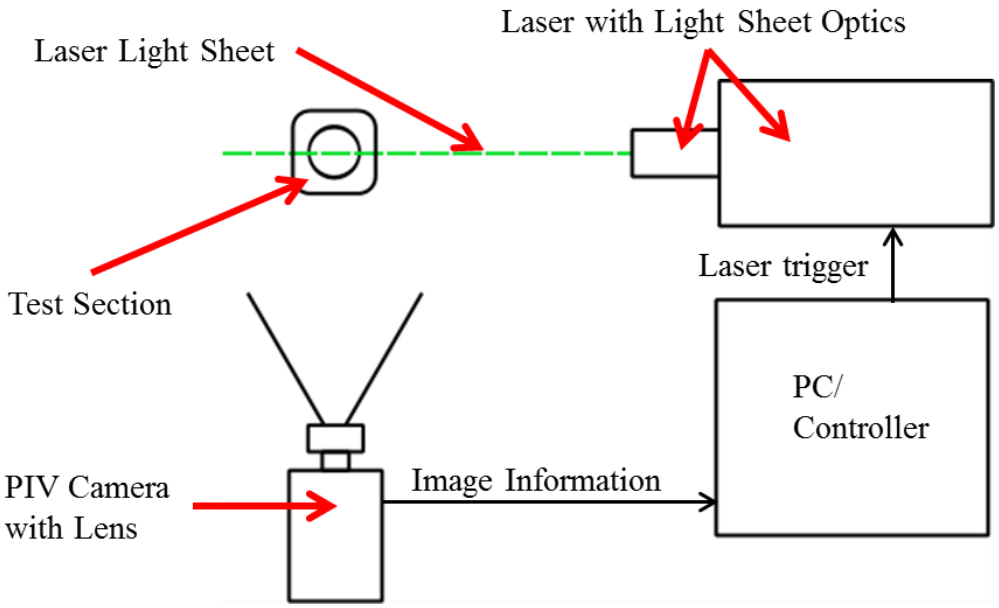

Figure 2.4 PIV setup schematic, shown from above.

The PIV camera captured images of the illuminated seed particles. Hollow glass spheres with a mean diameter of 10 µm were used as seed particles. The PIV camera accepted standard F-mount lenses as well as the long-distance microscope (LDM). 25 mm, 50 mm, and 60 mm lenses provided different zoom levels. In addition, extension tubes could be mounted between the camera and the lens to further increase magnification. The LDM provided the largest levels of zoom for the PIV camera. Appendix C details the lens and LDM specifications. A polarizing filter was also mounted on the end of the lenses to reduce undesired reflections. The

synchronizer controlled the timing of the image pairs captured by the PIV camera. These image pairs were transferred to the desktop computer for analysis.

2.5 High-Speed Camera

High-speed imagery provided by the high-speed digital camera was used to examine the two-phase flow structure details of the cavitation observed in the test section. Figure 2.5 shows the high-speed camera setup. The high-speed camera was equipped with an F-mount and was able to accept the 25 mm, 50 mm, and 60 mm lenses as well as the long-distance microscope (LDM). A fiber optic light source provided the backlight necessary for high framerate video capture. The fiber optic light source alone was too concentrated to properly illuminate the entire field of view for the high-speed camera. The addition of a pane of frosted glass diffused the light source over the entire field of view. The high-speed digital camera was controlled via a connected desktop computer running Photron FASTCAM Viewer. High-speed video was recorded into the camera's internal memory, where video segments were selected and downloaded to the desktop computer.

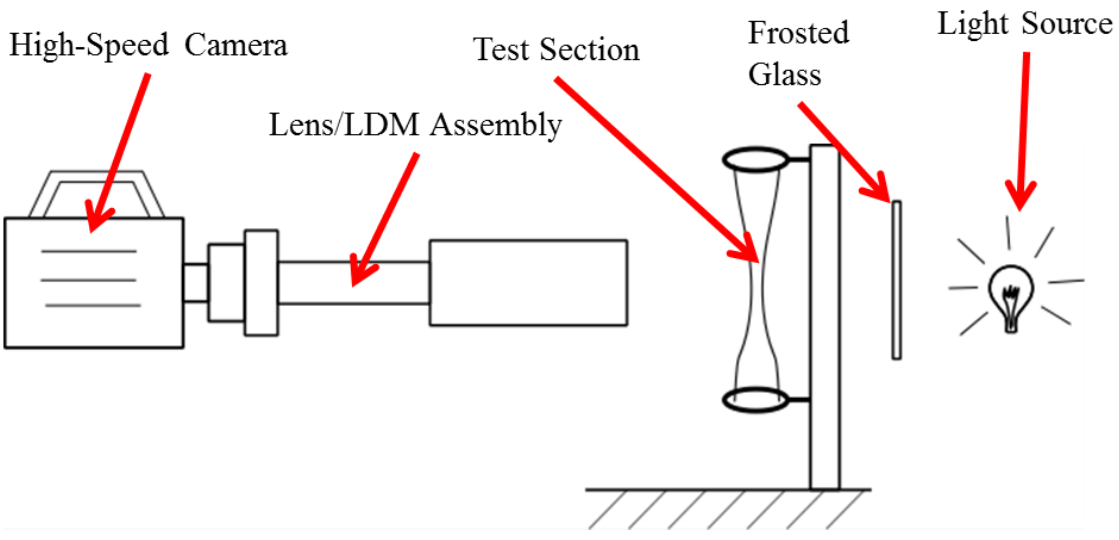

Figure 2.5High-speed camera setup with long distance microscope (LDM) attachment.

Chapter 3 - Experimental Procedure

All experiments focused on the water flow through the system test section. The basic procedure for controlling test conditions remained largely the same across all experimentation. Before any experiment began, water was supplied to the system. Depending on the quality (purity) of water needed, the supplied water sometimes required filtration. In other cases, the water was treated to remove dissolved gasses. After the water was supplied to the system from the upstream reservoir, care was taken to remove all air pockets that could disrupt the flow or cause surges in the system. These air pockets were removed by running the vacuum pump to create a small vacuum in the downstream reservoir and opening the ball valve connecting the downstream reservoir to the test section a minimal amount. Running the system at minimal flowrate allowed larger air pockets to be displaced (and subsequently carried out of the flow line) by liquid water coming from the upstream reservoir. The air pockets offered less resistance than the water inside the ball valve, and running the system at a minimal flowrate mitigated the surging when an air pocket reached the ball valve just upstream of the downstream reservoir. Large sections of the clear PVC tubing were manipulated (agitated) to release air pockets as well. After most air pockets had beenremoved, the flowrate was increased to further draw out any remaining air pockets. Larger flowrates were avoided until all air had been removed from the flow system.

3.1 Operation of Flow System

Once the upstream reservoir was filled and all air had been removed from the flow system, the system was ready for experimentation. For each new run of the system, the vacuum chamber was emptied of water to allow for the maximum working volume to be available for each experiment. With an empty vacuum chamber, the chamber pressure changedmore slowly

than when the chamber was partially filled with water. Once emptied, the vacuum chamber was isolated from the flow system by closing the ball valve connecting the chamber to the test section outlet and closing the ball valve on the bottom of the vacuum chamber. The ball valve between the vacuum chamber and the vacuum pump was then opened. The vacuum chamber pressure was lowered using the pump until the desired downstream pressure was reached. After reaching the desired pressure, the valve from the vacuum chamber to the pump was closed to ensure that no leaking flow could take place.

After the vacuum chamber pressure was prepared, flow was controlled by the ball valve connecting the vacuum chamber to the flow system. The valve had to be fully opened to expose the nozzle to the pressure of the vacuum chamber. In cases where fine control over the flow was needed, the valve was partially opened to throttle the flow. Throttling the flow was useful when it was desired to slowly approach conditions just before cavitation.

3.2 High-Speed Digital Camera

The first step in the high-speed setup was selecting the desired field of view. Next, a lens combination was selected that would accommodate the field of view. The selected lens or long distance microscope was attached to the high-speed camera and the camera was positioned on the movable camera platform, as shown in Figure 2.5. Positioning the camera was easiest with a low framerate and room lighting. After the selected field of view was established, the camera was visually focused on the test section using a low framerate and room lighting.

After the camera was aligned, a fiber optic light source was positioned behind the test section to provide sufficient lighting to support illumination at a high framerate. The fiber optic light source was used to backlight the test section with the aid of a pane of frosted glass to diffuse the light. In order to properly capture the details of cavitation, a framerate of at least

5,000 frames per second was found to produce clear (in focus) video with sufficient lighting. With a framerate less than 5,000 fps, traveling bubbles tended to appear blurred. Video was also taken at framerates up to 35,000 fps in order to visualize cavitation in the nozzle throat with a small field of view. The high-speed camera was calibrated whenever it was necessary to modify the camera framerate or the resolution. The camera was calibrated by covering the lens and rebalancing the brightness using the software controlling the camera on the desktop computer. Reducing the resolution of the high-speed camera reduced the memory requirement for each frame and allowed more frames to be saved during each capture sequence. By reducing the resolution to the section of interest, it was possible to extend the time duration of each high-speed capture. Detailed specifications of the high-speed camera are provided in Appendix B.

After the camera was calibrated for the selected resolution and framerate, fine adjustment of the focus and positioning was done with the flow on. Adjusting the focus with flow on allowed the focal plane to be adjusted to different locations in the test section, such as at the wall nearest the camera or at the midplane of the test section. With the high-speed camera suitably focused on the section of interest, the flow system was set to the required parameters and high-speed video capture was triggered through the camera control software. The camera captured raw video until the internal memory of the camera was filled. The high-speed camera used was able to capture full resolution (1,024 x 1,024 pixels^2) at a framerate of 7,000 fps for 0.780 seconds. After the triggered capture, sections of the raw capture were saved to the desktop computer controlling the camera for later analysis.

3.3 PIV System

The PIV camera and laser were set up perpendicular to the water flow through the test section, as shown in Figure 2.4; this orientation rendered out-of-plane motion of the seed

particles insignificant. With insignificant out-of-plane motion, classic (mono) PIV worked well and reduced the complexity of the experimental setup. The PIV camera was attached to the movable camera platform as shown in Figure 2.3. An appropriate lens combination was selected to focus on the desired field of view. Standard F-mount lens were compatible with the PIV system. Extension tubes were used in some experiments to increase the optical zoom when needed. A long distance microscope also provided a large optical zoom (field of view of 2.5 x 2.5 mm^2); however, the long distance microscope increased the difficulty in focusing on seed particles in the test section. Alignment and course focus adjustment of the camera was done with room lighting and no laser. After the camera was in place and focused, the laser was also aligned with the test section. The light arm, scissor-jack, and linear stage attached to the laser optics were used to position the laser light sheet in the desired plane of the test section, as seen in Figure 2.4. If necessary, the waist of the laser light sheet was focused on the center of the desired field of view. The waist of the light sheet was focused using the sheet focus adjustment included in the light sheet optics component. Stray, diffuse reflections of the laser light into the camera were minimized as much as possible with the addition of a polarizing filter to the end of the lens on the PIV camera. The polarizing axis was rotated to minimize reflections off the nozzle glass into the camera.

Next, the introduction of seed particles allowed for fine focus adjustment of the PIV camera. Glass microspheres, 10 μm diameter, were injected into the flow system using a wash bottle containing a highly concentrated mixture of seed particles and water at the exit of the upstream reservoir to seed the flow. Manually injecting the seed particles at the exit of the upstream reservoirallowed for precise control of the seed density entering the test section. Once the seed particles reached the test section and were illuminated by the laser light sheet, the

particles presented small targets that allowed for fine focus adjustment of the PIV camera. The laser light intensity was also adjusted at this point to allow as much light into the camera as possible without saturating the camera sensor array. The laser light intensity was also adjusted between the two lasers to produce the same light intensity in both frames of the PIV capture. The timing delay between frames was modified to meet the needs of the flow field under interrogation. A small field of view with a high flow velocity necessitated a smaller time step than did a larger or slower field of view.

Once all the parameters of the PIV system were calibrated to the desired field of view, the system was ready to capture the raw flow field data. During calibration and setup, many single PIV captures were recorded to check for proper calibration. Once quality captures were ready to be recorded, the flow system was prepared to make flow conditions as steady. First, the desired test section inlet and outlet pressures were established. Then, seeding the flow was started and adjusted to reach the optimum seed density in the test section. The optimum seed density depended on the field of view. For valid flow field velocity vectors to be determined, at least five seed particles were needed within each interrogation cell. For a small field of view, higher seed density was needed to provide the requisite number of seed particles in each cell. If seed density was too high, the light scattered by each seed particle would interfere with its neighbors and speckling would occur. Once sufficient seeding was established, the PIV software was triggered to record the desired sequence of captures. The captured image pairs were then reviewed before being saved to the hard drive for future processing. After the desired images were saved to the PC's hard drive, the images were processed using Insight 4G software to produce velocity vector fields. The produced vector files were then stored and made available for further processing on the PC running the Insight 4G software.

Chapter 4 - Experimental Results

Experimental results obtained from the test facility, previously described in chapter two, are presented in this chapter. The Particle Image Velocimetry (PIV) and high-speed digital camera experimental data gathered represent a huge quantity of raw data; thus, the results presented in this chapter are a summary of findings and observations from the aforementioned data. Pressure and water flowrate data for Nozzle-1 and Nozzle-2 are also presented in this chapter. For Nozzle-1, volumetric flowrate data was recorded for a range of pressures in the vacuum chamber downstream from the test section. In addition to regulating the back pressure, two different pressures, controlled by the upstream reservoir elevation, were applied to the test section inlet. For Nozzle-2, a range of back pressures wasused at the test section outlet to evaluate water flow characteristics within the test section. The test section outlet pressure was controlled by the downstream reservoir and connected vacuum pump. The addition of a pressure transducer immediately before and after the test section allowed for the collection of additional pressure data for Nozzle-2. This additional data was related to the investigation of pressure drop characteristics associated with the flow between the nozzle exit and the downstream reservoir.

4.1 Effects of Pressure on Flowrate

The water flow through the system and test section was controlled by adjusting the pressures on the inlet and outlet of the test section. The inlet pressure was set by the elevation of the upstream water reservoir. The elevation of the reservoir was not frequently changed; therefore, the test section outlet pressurewas the primary control for the water flowrate. The water level of the upstream reservoir was small for each run of the system and varied less than 14 cm throughout testing (less than 1.4 kPa change at test section inlet). The test section outlet pressure was controlled using the vacuum chamber located downstream of the test section andthe

ball valve connecting the test section outlet and vacuum chamber. A rotameter measured the water volumetric flowrate, located immediately before label 2 in Figure 2.1.

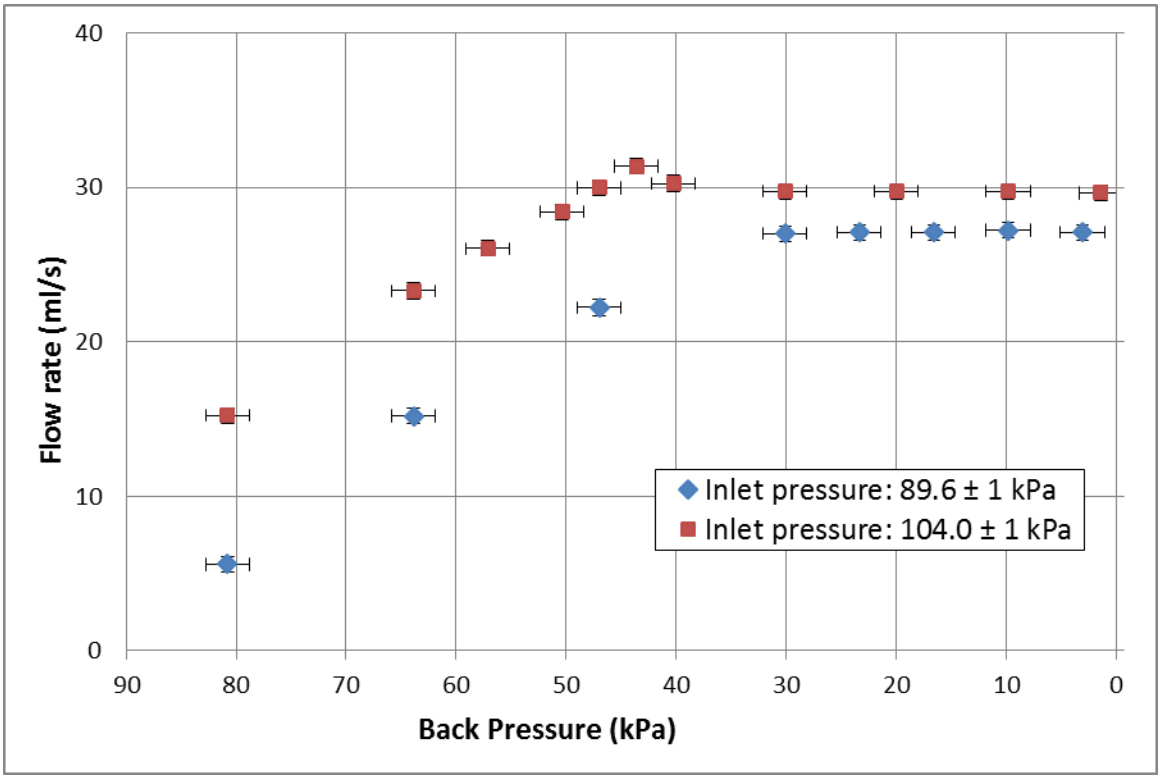

Figure 4.1Pressure effects on flowrate for Nozzle-1. Inlet absolute pressure measured with liquid-filled pressure gauge and barometer.

Two test section inlet pressures were applied to Nozzle-1and the water flowrate was recorded for a range of outlet pressures. Figure 4.1 shows the measured flowrate for each outlet pressure. For each test section inlet pressure, the flowrate within the nozzle increased approximately proportional to the test section outlet pressure until a flowrate threshold was reached and cavitation was initiated. After a maximum flowrate was reached, lowering the outlet pressure had no further effect on the flowrate. The maximum flowrate was affected by the test section inlet pressure. Figure 4.1 shows that changing the inlet pressure effects the maximum flowrate. At a back absolute pressure of 44 kPa and an inlet absolute pressure of 104.0 kPa, a flowrate higher than the threshold was achieved. At this back pressure, cavitation did not always

occur. When cavitation did occur at this back pressure, the flowrate would snap down to the flowrate threshold; when cavitation did not occur, a higher flowrate than the threshold was reached. The sudden drop in flowrate was a result of a sudden pressure rise, and corresponding velocity decrease according to Bernoulli's principle, in the nozzle throat. This snapping effect suggests the water flow in the nozzle was metastable, below the vapor saturation pressure, prior to cavitation initiation.

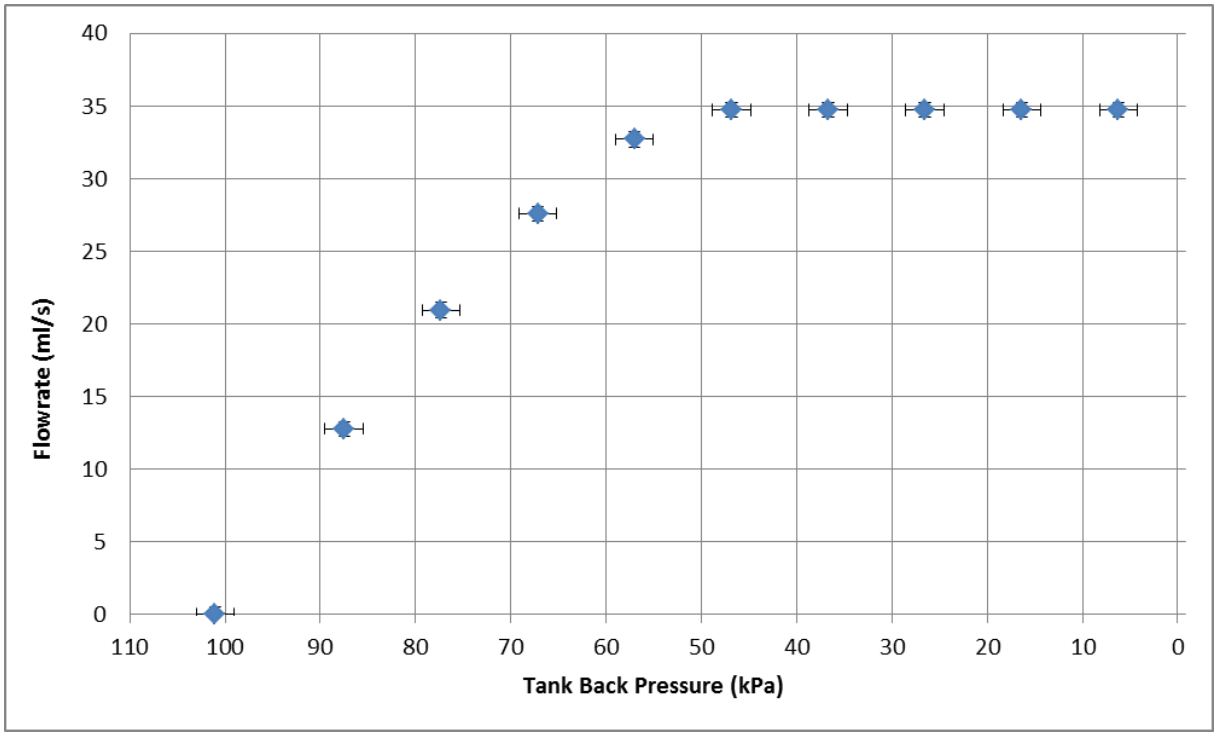

Figure 4.2Pressure effects on flowrate for Nozzle-2. Inlet absolute pressure of 104.0 ± 1 kPa measured with liquid-filled pressure gauge and barometer.

Nozzle-2 exhibited similar behavior as Nozzle-1. The upstream reservoir was elevated to produce a test section inlet pressure of 104.0 kPa. As with Nozzle-1, the flowrate within Nozzle-2 increased as the test section outlet pressure decreased, as shown in Figure 4.2. After a maximum flowrate of 35 ml/s was reached, reducing the test section outlet pressure had no effect on the flowrate. The maximum flowrate of Nozzle-2 for an inlet pressure of 104.0 kPa at 35 ml/s was greater than the maximum flowrate of Nozzle-1 at the same inlet pressure of 30 ml/s. This

was due to the larger throat diameter of Nozzle-2. As with Nozzle-1, the flowrate was dependent upon the outlet pressure until cavitation occurred. After cavitation occurred, the flowrate became independent of the test section outlet pressure. This behavior was consistent with choked flow that occurs in single-phase gas flow through a nozzle when sonic conditions are reached at the nozzle throat.

With Nozzle-1, only the downstream reservoir pressure was measured. The test section inlet pressure was calculated based on the elevation difference between the test section and the upstream reservoir, accounting for pressure losses from friction. The test section outlet pressure was assumed to be close to the vacuum chamber pressure as there are no elevation changes and little frictional losses. With Nozzle-2, pressure transducers at the test section inlet and outlet allowed for direct measurement of pressures immediately before and after the test section. Figure 4.3 shows the pressure measurements of the test section inlet and outlet as well as the vacuum chamber pressure for Nozzle-2.

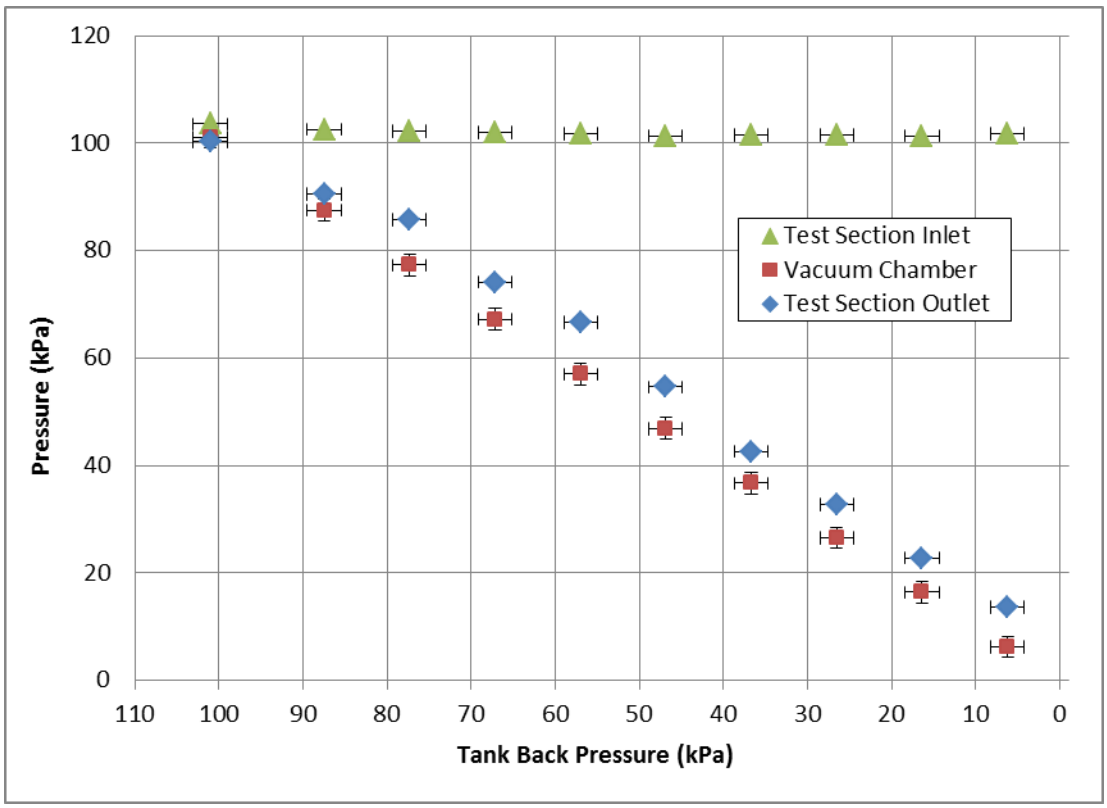

Figure 4.3Comparison of vacuum chamber and test section absolute pressures for Nozzle-2. Test section inlet and outlet pressures measured with pressure transducers. Vacuum chamber pressure measured with dry pressure gauge and a barometer.

Figure 4.3 shows that the test section inlet pressure does not change significantly over the range of downstream reservoir pressures tested. The pressure measurements from the test section outlet and downstream vacuum chamber were 100.3 ± 0.08 kPa and 101.0 ± 2 kPa, respectively, at no flow conditions; while the test section inlet was 103.5 ± 0.2 kPa due to the head pressure provided by the elevated upstream reservoir. The test section inlet pressure dropped to 101.5 kPa at maximum flow due to dynamic pressure effects. The test section outlet and vacuum chamber pressures were decreased to drive higher flow through the system. As flowrate increased, the difference between the test section outlet and vacuum chamberpressures, plotted as "Downstream Pressure Drop" in Figure 4.4, increased to a maximum difference of 7 kPa as the maximum flowrate was reached and cavitation occurred. The relationship betweenthe

test section outlet pressure and the vacuum chamber pressure is consistent with a pressure drop that was a function of flowrate, increasing to a maximum once cavitation cause the flow to choke.Figure 4.4 also shows the pressure drop from the test section inlet to the test section outlet, plotted as "Nozzle Pressure Drop." The pressure drop within the nozzle continued to increase with decreasing downstream reservoir pressure, after cavitation initiated and flowrate remained choked.

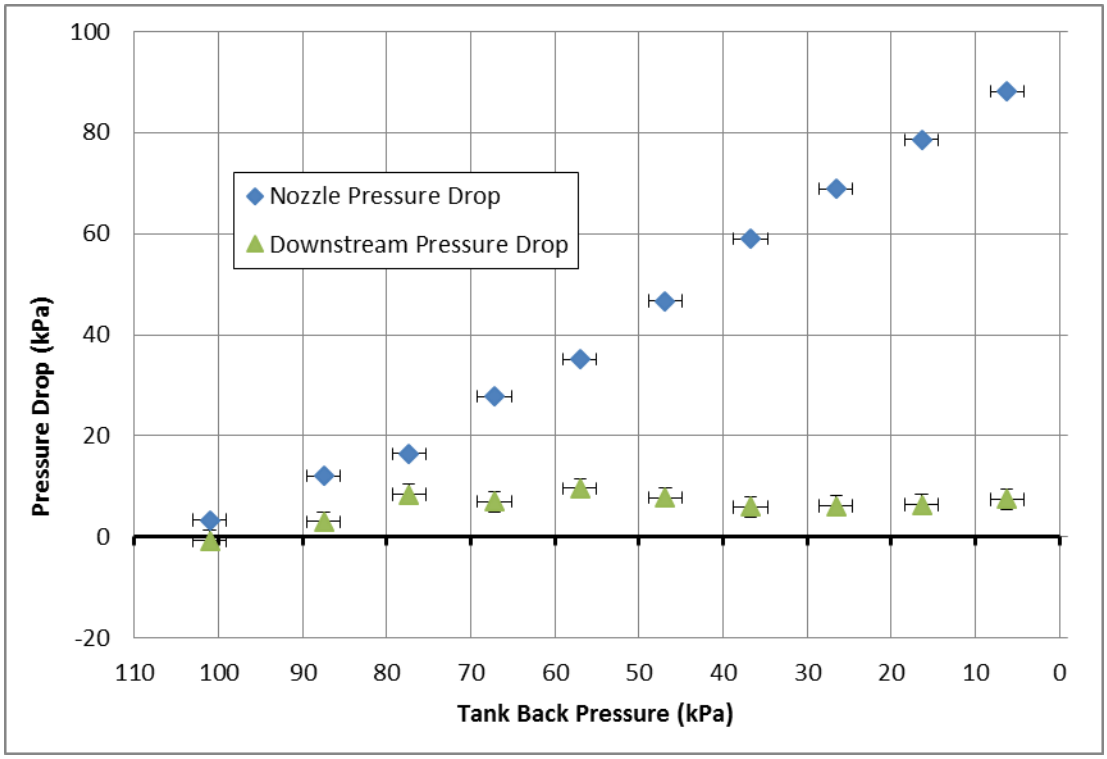

Figure 4.4 Measured pressure drop from test section inlet to outlet (nozzle pressure drop) and from test section outlet to downstream reservoir (downstream pressure drop) for Nozzle-2.

Flowrate data from Nozzle-1 and Nozzle-2 both exhibited characteristics of choked flow. The flowrate through the nozzle was dictated by the pressure drop across the nozzle until choked conditions occurred in the nozzle. After chocked flow occurs in the nozzle, decreasing the downstream pressure had no effect on the flowrate. After chocked flow was established, only increasing the upstream pressure would drive higher flowrate through the nozzle. This choked

behavior suggests sonic conditions were reached within the nozzle and coincided with the onset of cavitation. The "snapping" of the flow down to the choked flowrate level after exceeding the cavitation onset suggests that water within the nozzle was metastable until cavitation initiated. After cavitation was established, the flowrate had to be lowered below the point of initiation to arrest cavitation. This behavior also suggested metastable conditions were reached before cavitation occurred.

4.2 High-Speed Flow Visualization

The FASTCAM SA5 high-speed digital camera was used to visualize the cavitating flow through the nozzle test sections as well as to measure some quantitative characteristics of the flow through these nozzles. The high-speed camera was used at a number of different framerate modes, which ranged from still image captures at framerates as low as 60 frames per second (fps) to high-speed flow visualization captured at framerates up to 35,000 fps. Low framerates were used to capture static images within Nozzle-1. These still images were used to measure the interior nozzle shape profile and provided the calibration data needed to convert pixel-space distances and velocities into real-world positional and velocity data. High-speed video ranging from 1,000 fps to 35,000 fps was used for flow visualization, as well as velocity measurement.

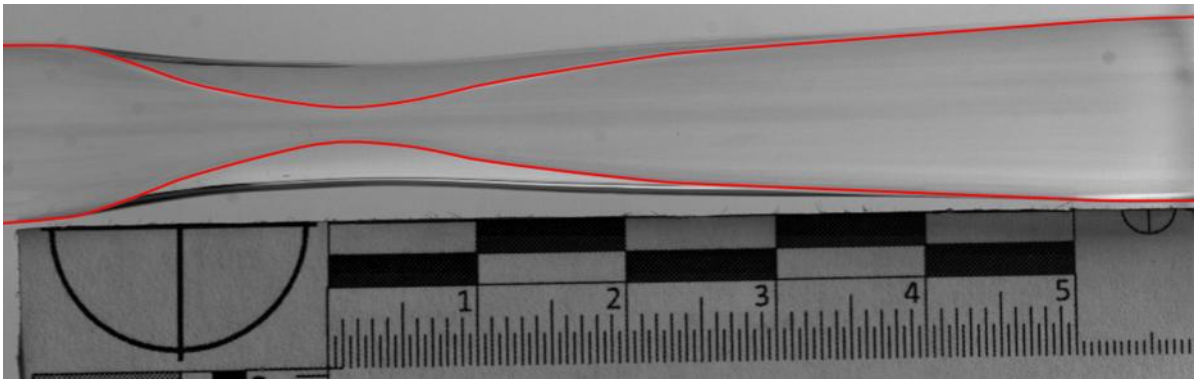

Figure 4.5 Nozzle-1 with scale in cm. Interior of nozzle outlined for emphasis.

The high-speed digital camera with a standard F-mount lens was used to visualize the interior surface profile of Nozzle-1, as shown inFigure 4.5. Nozzle-1 was filled with water to minimize distortions along the interior wall, while still allowing the wall to be visible. The interior wall has been outlined for clarity. A centimeter scale was positioned next to Nozzle-1 and aligned with the midplane of the nozzle. The scale provided a two-dimensional calibration for the image and allowed pixel data to be mapped into real distances (mm). The positional data of the outlined interior wall from Figure 4.5 was used to measure the nozzle diameter at different axial positions. The nozzle diameter was plotted against the axial position relative to the nozzle throat, as shown in Figure 2.2. The curved surface of Nozzle-1's exterior distorted the viewing of the interior. The raw optical measurements had considerable error when compared to physical measurements at the nozzle's inlet, outlet, and throat. A linear correction has been applied to the diameter data presented in Figure 2.2 C to correct for optical distortions and produce correct inlet, outlet, and throat diameters measured from Nozzle-1. A series of cylindrical rods were used to gauge the throat diameter. The inlet and outlet diameters were measured with a caliper. These measurements were used to define a corrected diameter based on the optically measured diameter. The inlet and throat diameters were used as boundary conditions for the linear correction.

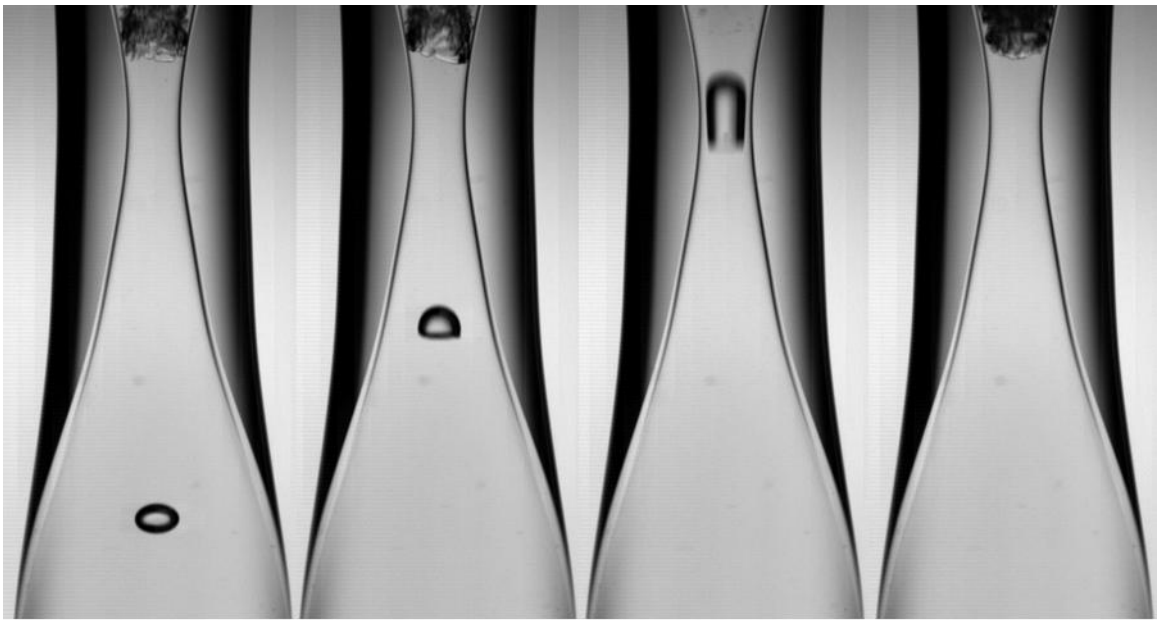

Figure 4.6 High-speed video of bubble in converging section of Nozzle-1 with a vacuum chamber absolute pressure of 30 ± 2 kPa.

High-speed video was taken of the converging section of Nozzle-1, shown in Figure 4.6. The displacement of an injected bubble was tracked as it traveled through the nozzle throat. The pixel positional data was converted into real length data using a two-dimensional calibration based on the known nozzle throat diameter. The bubble velocity was calculated using this positional data along with time information provided by the high-speed digital camera. The velocity of the bubble increased from 0.4 m/s before entering the converging section of Nozzle-1 to about 14 m/s in the throat region. Velocities near the throat were difficult to discern due to the elongation and distortion of the bubble, shown at 5.70 ms in Figure 4.6. Tracked bubbles that had diameters comparable to the nozzle throat disrupted the downstream cavitation, shown at 5.70 ms in Figure 4.6. The peak velocities of measured bubbles agreed with the averaged throat velocity of 14 m/s based on measured flowrate and throat cross-sectional area. The throat diameter of Nozzle-1 was initially estimated to be 2.3 mm. Later, when the flow visualization

measurements were found not to be consistent with the flowrate measurements of the nozzle throat velocity, the measurement technique used to determine the nozzle throat diameter was scrutinized. This led to a more reliable method of measuring Nozzle-1's throat diameter, which broughtthe observed throat velocity bubble measurement in line with the throat velocity determined from the (rotameter) measured volumetric flowrate.

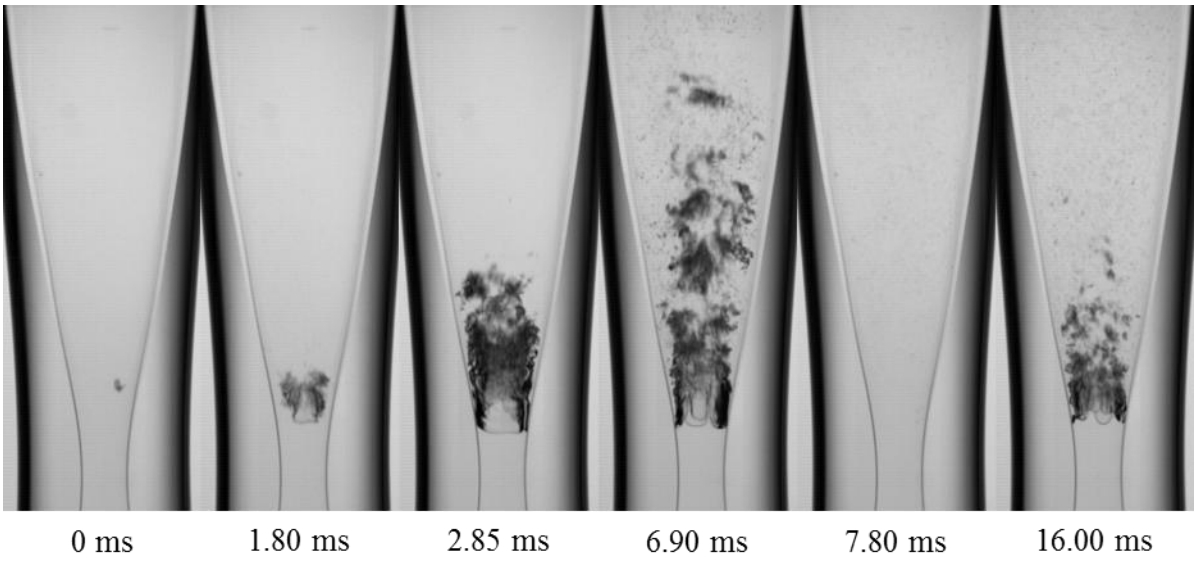

Figure 4.7Cavitation onset in Nozzle-1 with a vacuum chamber absolute pressure of 27 ± 2 kPa. Time of images indicated in milliseconds.

The high-speed digital camera was used to visually capture the onset of cavitation in the test section. Figure 4.7 shows the onset of cavitation in Nozzle-1 with a vacuum chamber pressure of 27 ± 2 kPa. This represented a change in pressure from the test section inlet to the test section outlet that was just large enough to reliably trigger cavitation. Cavitation was initiated past the nozzle throat and began as a small void. This void expanded across the nozzle cross-section in about 2 ms. The void region then grew in length until sections of the void began breaking away from the initial void and traveled downstream from the nozzle throat around 3 ms after the voids were first observed. These large void regions were produced until about 7 ms after the onset of cavitation. From 7 ms to 8 ms after cavitation onset, the cavitation front

completely collapsed. Figure 4.7 shows the time at which the cavitation front had completely collapsed, 7.80 ms after the onset of cavitation. After the cavitation front collapsed, cavitation restarted and reached a steady-state 16 ms after the onset of cavitation. The cavitation front only collapsed one time before continuing to reach a steady form of cavitation.

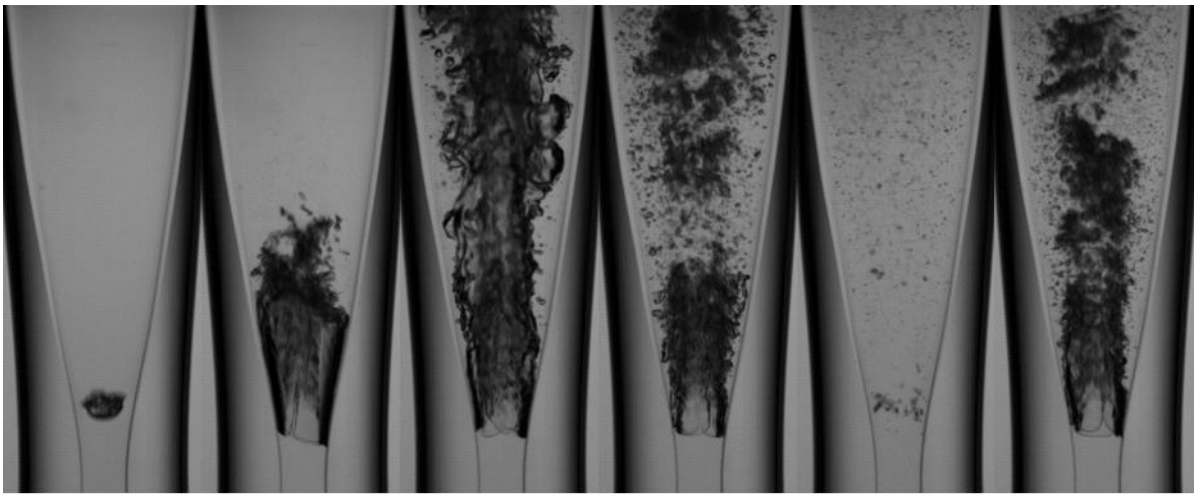

Figure 4.8Cavitation onset in Nozzle-1 with a vacuum chamber absolute pressure of 9.6 ± 2 kPa. Time of images indicated in milliseconds.

Figure 4.8 shows the onset of cavitation for a lower vacuum chamber pressure of 9.6 ± 2 kPa. The lower vacuum chamber pressure consequently produced a larger pressure difference from the test section inlet to the test section outlet. At 0 ms in Figure 4.8, the bubble shows the initiation of the void expanse at the same axial location previously observed at 0 ms in Figure 4.7. The void expanded faster in Figure 4.7 than in Figure 4.8 and continued to grow for a longer time, covering a larger area of the nozzle diverging section. Figure 4.8 shows that the cavitation front began to collapse around 70 ms after cavitation onset. At 75.14 ms after cavitation onset, the cavitation front had completely collapsed. After 96.34 ms, the cavitation front had reestablished and reached a steady-state. The pattern of void initiation, expansion, collapse, and reestablishment was observed for each high-speed video capture of cavitation

onset. This behavior, along with the rapid drop in flowrate accompanying cavitation onset, suggested that a metastable state was reached in the region of the throat. This metastable flow allowed the flowrate to exceed the stable maximum flowrate. Once cavitation was initiated, the flowrate quickly dropped to the maximum stable flowrate, shown in Figure 4.1. This sudden drop in flowrate caused the cavitation voids to momentarily collapse before steady-state conditions were then established.

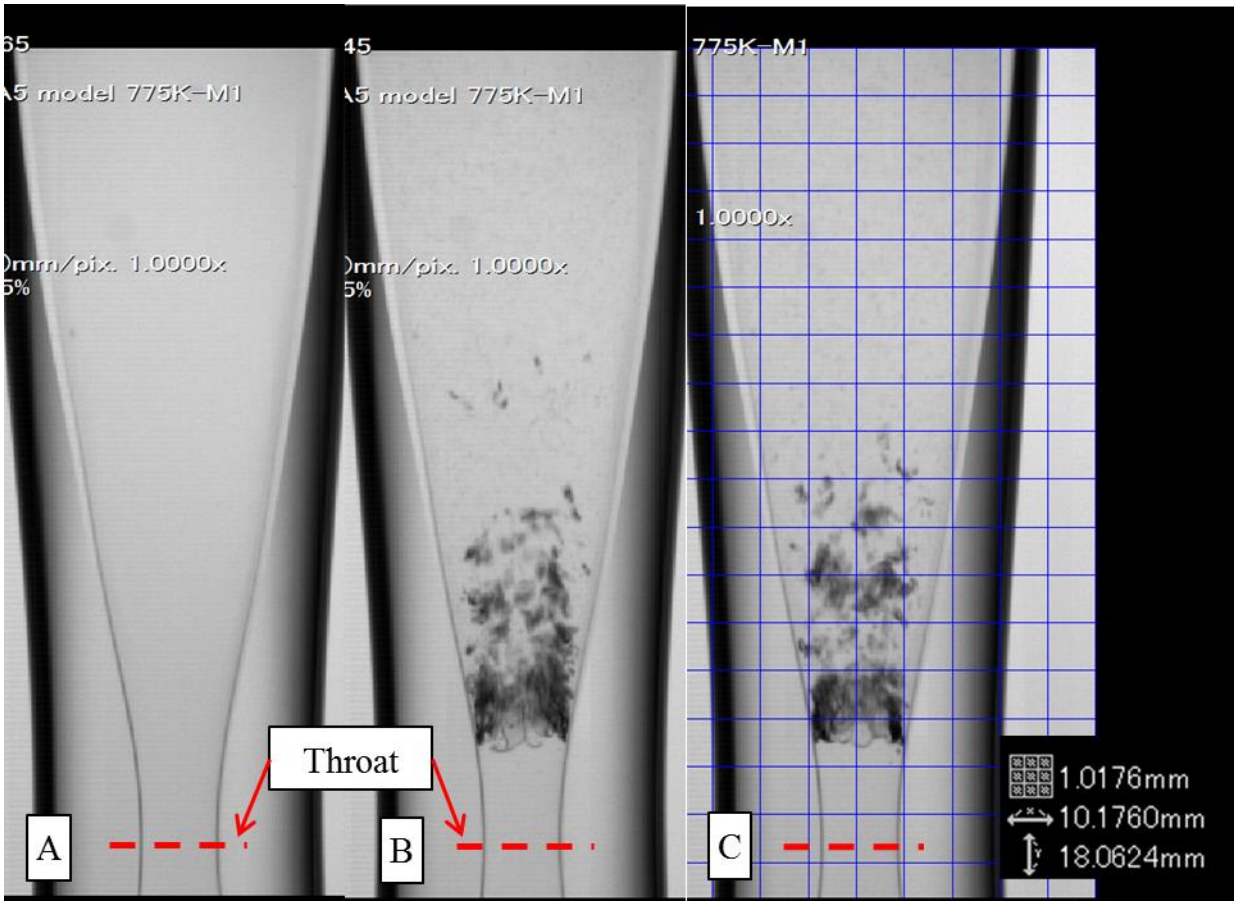

Figure 4.9High-speed video of Nozzle-1 throat and diverging regions. Flow shown just before cavitation (A), with cavitation (B), and with cavitation and graduated grid (C).

The onset of cavitation was initially expected at the minimum pressure of the test section. If the flow through the test section were inviscid, the pressure minimum would occur at the velocity maximum, assuming single-phase flow through the test section and negligible change in

elevation. In single-phase flow, with no flow separation, the maximum velocity would be expected to occur at the nozzle throat; therefore, cavitation was expected to initiate at the nozzle throat. Figure 4.7 and Figure 4.8 show that both the onset of cavitation and the established cavitation front occurred past the nozzle throat. Figure 4.9 shows the location of the cavitation front in relation to the nozzle throat. The grid spacing of 1.02 mm in Figure 4.9 indicated the cavitation front occurred approximately 2 mm downstream of the nozzle throat. The location of the cavitation front was mostly static once the transient behavior associated with the onset of cavitation had passed. The length of the cavitating region increased at lower test section outlet pressures. Lower test section outlet pressures also shifted the cavitation front approximately 0.5 mm upstream to approximately 1.5 mm downstream of the nozzle throat. This slight shift can be seen in Figure 4.10 or when comparing Figure 4.9 and Figure 4.10. This phenomenon was also observed in PIV measurements interrogating the cavitation front with small fields of view (3 mm x 3mm).

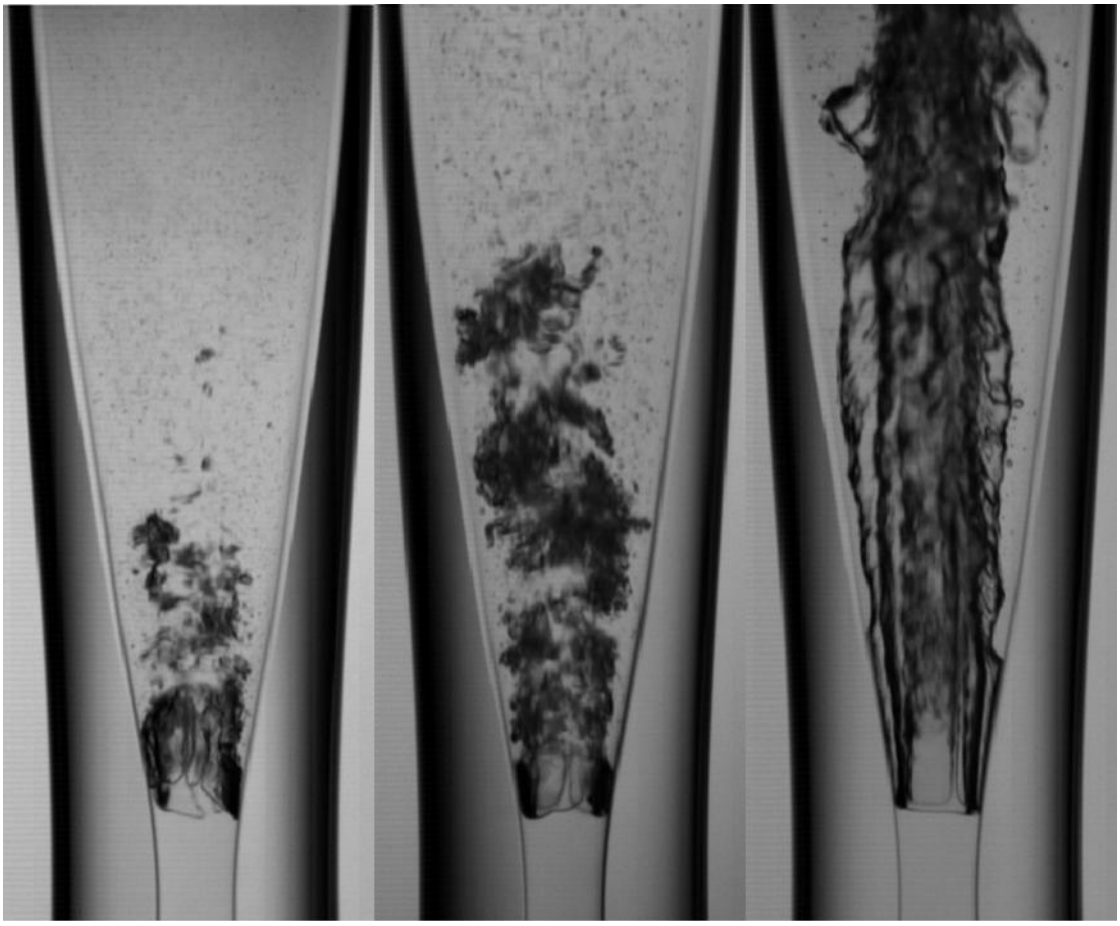

Figure 4.10Cavitation length shown at different vacuum chamber absolute pressures for Nozzle-1.

Section 4.1 shows that, once cavitation was initiated, the flowrate through the test section was independent of the test section outlet pressure for outlet pressures below the minimum cavitation pressure level. Figure 4.10 shows that the test section outlet pressure did affect the length of the cavitation region. For a vacuum chamber absolute pressure of 27 kPa, the test section outlet pressure was just low enough to initiate cavitation and the cavitation length was minimized. A lower vacuum chamber pressure of 13 kPa produced a longer cavitation length, while a vacuum chamber pressure of 1.1 kPa created a cavitation region that spanned the length of Nozzle-1's diverging section, shown in Figure 4.10. The minimum test section outlet

pressure, corresponding to a vacuum chamber pressure of 1.1 kPa, produced large void regions surrounding a central jet of liquid water. The void regions that surrounded the jet were transient and would collapse and return in a cyclical behavior. The cyclical behavior of these void regions was only apparent in the high-speed video when viewed with framerates greater than 10,000 fps.

The effect of test section outlet pressure on the cavitation length suggests that the pressure information was transmitted as far upstream as the region near the cavitation front. The pressure information from the test section outlet was not transmitted to the throat, as the velocity at the throat remained constant once cavitation was initiated. Had the information reached the throat, the throat velocity would have increased, which would have been observed as an increase in flowrate. The failure of the pressure information transmission from the test section outlet to the throat suggested that a sonic condition was present somewhere between these two points. This is another characteristic of choked flow in a converging-diverging nozzle, and appears to be roughly similar to the behavior for single-phase choked flow.

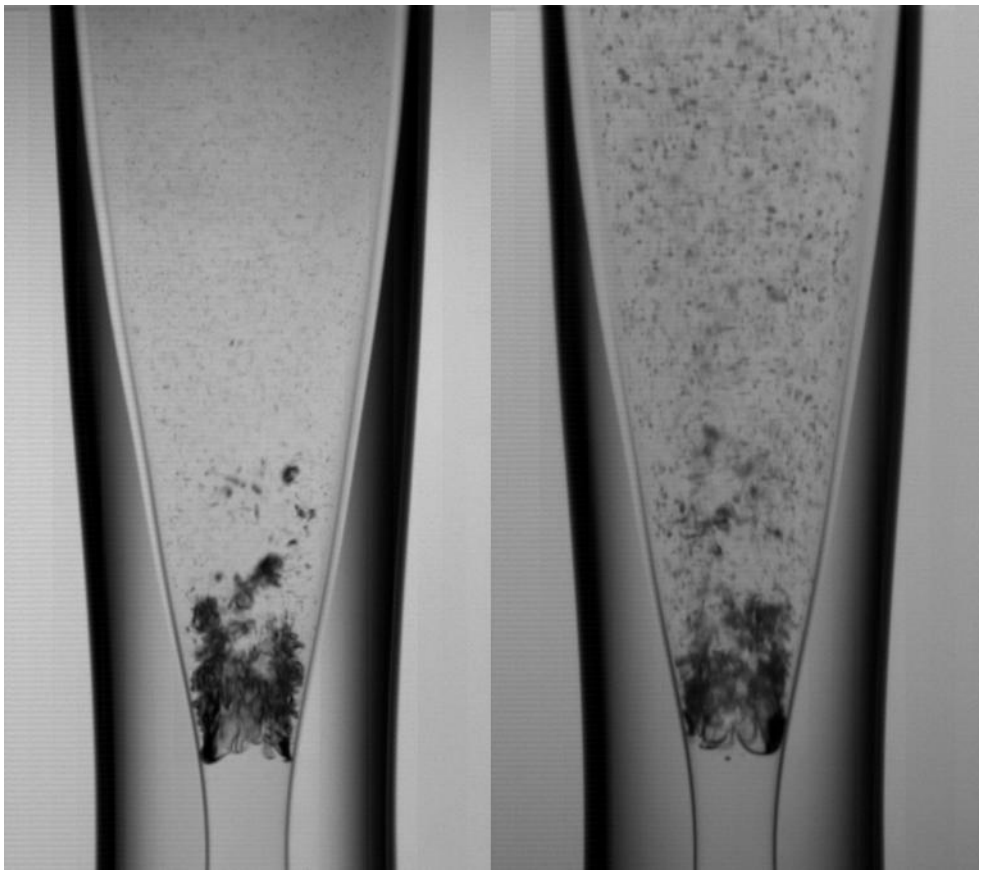

Figure 4.11Cavitation in Nozzle-1 with a vacuum chamber absolute pressure of 27 ± 2 kPa with degassed water (left) and tap water (right).

The possible effect of dissolved gasses in the water used in the system was explored. The concentration of dissolved oxygen was measured using a chemical dissolved oxygen test kit. Tap water, which was used for the majority of experimentation, was measured between 7 and 8 parts per million (ppm) of dissolved oxygen. The concentration of dissolved gasses in the water was reduced by exposing the water to a vacuum for at least an hour. Holding the water under a vacuum for this period of time reduced the dissolved oxygen concentration to 1 ppm. Cavitation was captured using the high-speed digital camera for both degassed and tap water, shown in Figure 4.11. Degassing the water reduced the size of persistent bubbles in the diverging and downstream sections of the test section. Degassing the water did not affect the cavitation length

or the test section outlet pressure required to initiate cavitation. At lower test section outlet pressures, there was no difference observed between degassed and tap water.

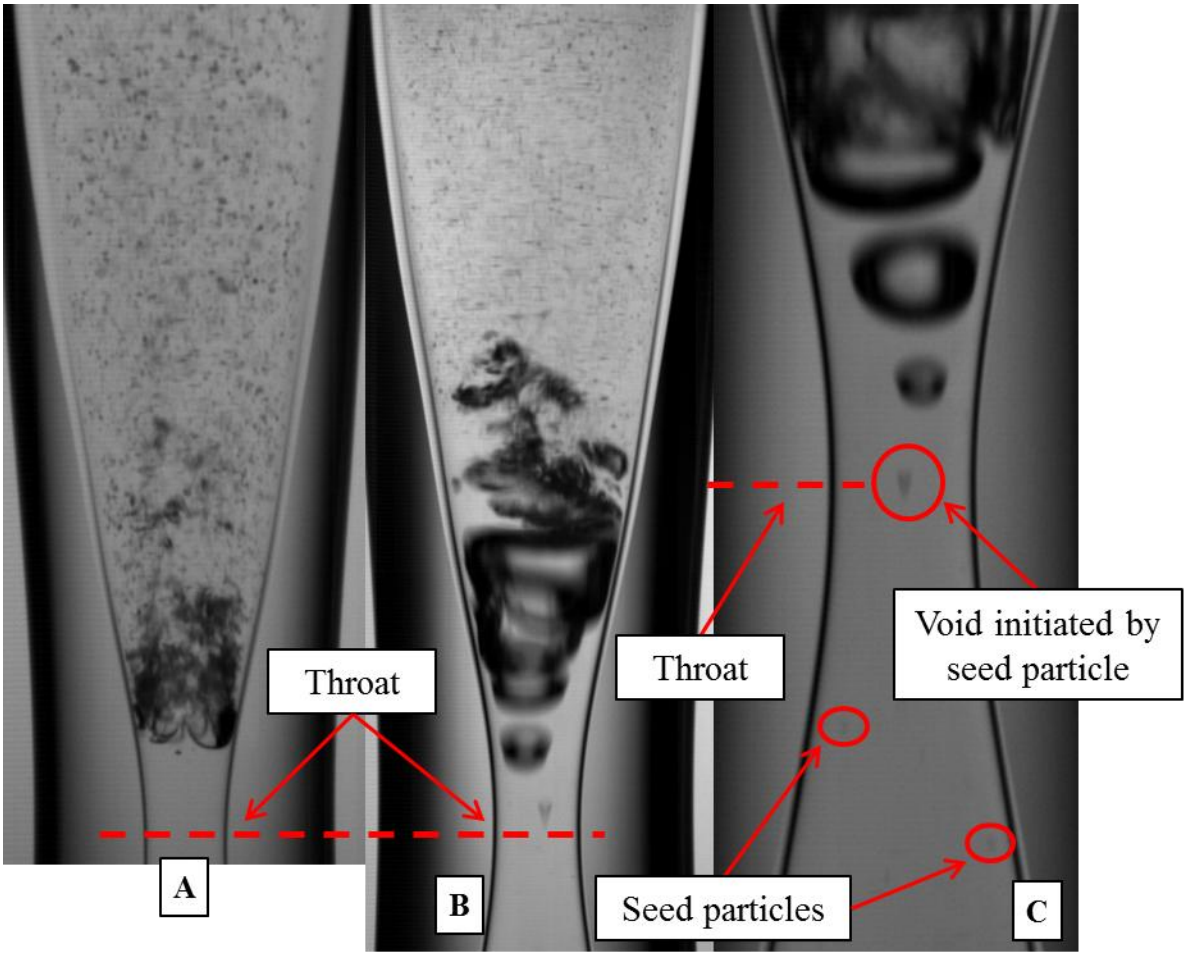

Figure 4.12Normal cavitation in Nozzle-1 (A). Seed induced cavitation in Nozzle-1 (B). Detailed view of seed induced cavitation in Nozzle-1 (C). Vacuum chamber absolute pressure of 27 ± 2 kPa. Spherical 120 µm diameter glass seed particles.

Particle Image Velocimetry required the introduction of seed particles into the water flow through the system. Each seed particle provided a potential activation site for cavitation. Hollow glass spheres with a mean diameter of 10 µm were used for PIV seeding. No difference in cavitation behavior was observed with the 10 µm glass seed particles. Glass spheres with a mean diameter of 120 µm were also tested in the flow system. Figure 4.12 shows the effect the 120 µm glass sphere had on the cavitation behavior. The 120 µm glass sphere provided

activation sites for cavitation. These spheres promoted cavitation starting at the nozzle throat. The expanded view of Figure 4.12 shows that the cavitation voids were initiated from seed particles as the seed particles traveled through the nozzle throat. Figure 4.12 indicates that conditions for cavitation were present at the nozzle throat. When sufficient activation sites were available, cavitation did occur at the throat. Without activation sites, the flow did likely travel past the throat, in a metastable state, and cavitate some distance downstream from the nozzle throat.

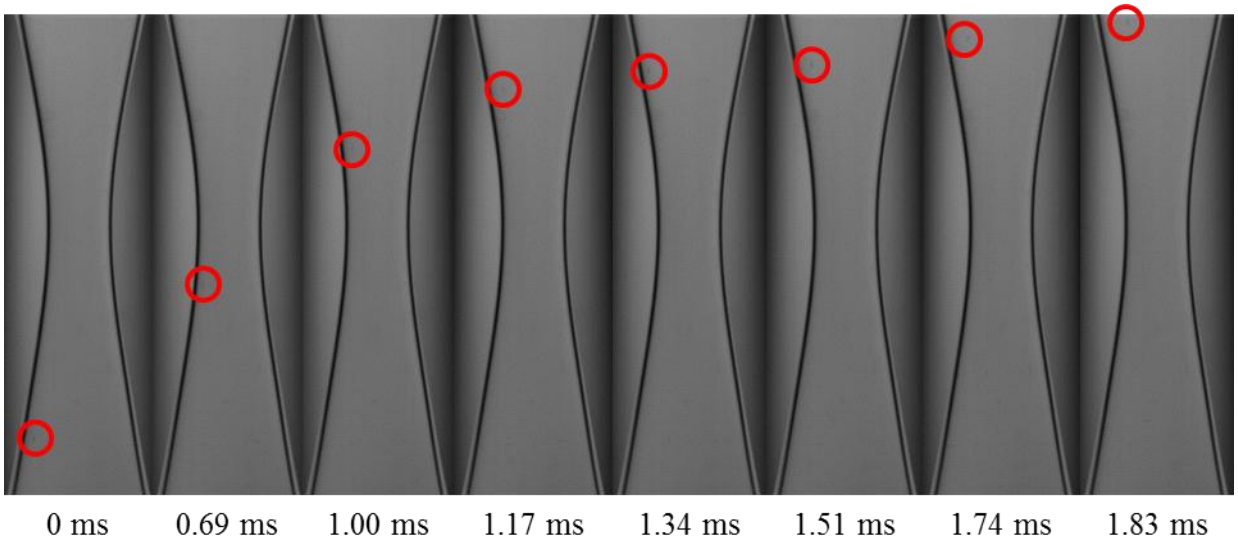

Figure 4.13Recirculation of seed particle in Nozzle-1 with vacuum chamber absolute pressure of 49 ± 2 kPa.

The 120 μm glass spheres were visible by the high-speed digital camera with sufficient framerate and zoom. High-speed images presented in Figure 4.13 tracked one glass sphere as it traveled through Nozzle-1's throat. The test section outlet pressure was kept high enough to avoid cavitation so the particle could be tracked through the entire throat region. The seed particle entered the frame from below and quickly traveled parallel to the nozzle wall, through the throat. At 1.17 ms, the seed particle appeared to stop. From 1.17 ms to 1.51 ms, the seed particle drifted in a lateral motion, tangent to the nozzle flow. At 1.74 ms, the seed particle

rejoined the fast moving jet flow in the center of the nozzle and left the top of the frame after 1.83 ms. The seed particle path suggested an area of slower flow near the nozzle wall, downstream from the throat.

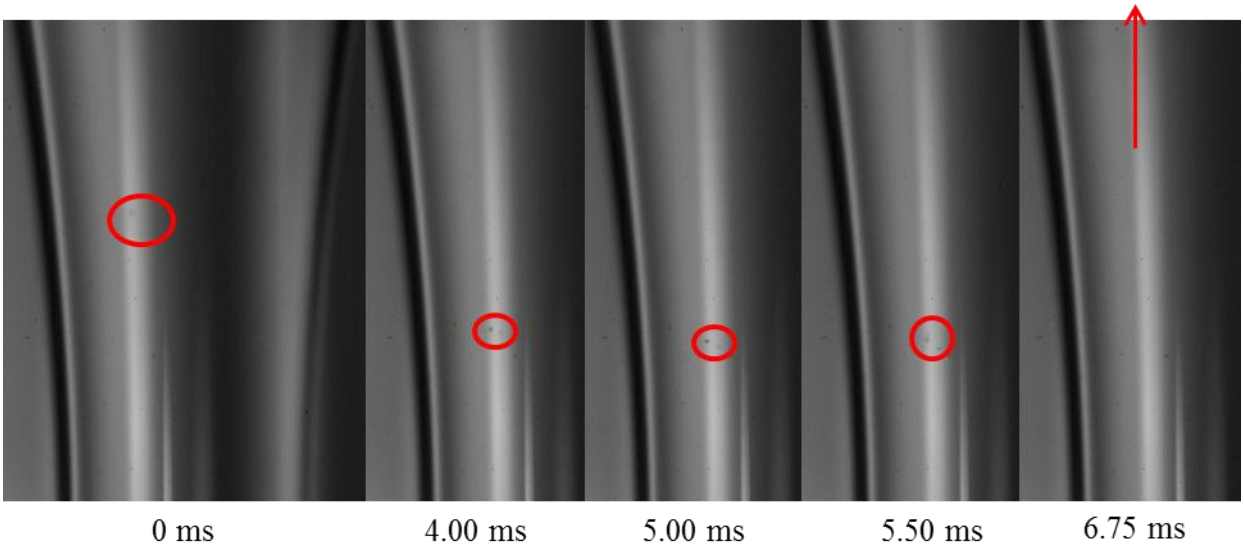

Figure 4.14Close view of recirculation of cavitation bubbles immediately downstream of throat in Nozzle-1.

Bubble tracking was also used to visualize the fluid flow in the region immediately downstream of Nozzle-1's throat. Figure 4.14 highlights two bubbles that were produced from cavitation in the nozzle and were carried back upstream by reversed flow near the nozzle wall. At 0 ms in Figure 4.14, the two bubbles were traveling down in the frame, against the bulk flow of the nozzle. From just after 0 ms to 5.00 ms, the bubbles attached to the nozzle wall and increased in size. At 5.50 ms, the bubbles detached from the nozzle wall and began traveling upward, carried by the central jet flow of the nozzle. By 6.75 ms, both bubbles had traveled up, out of frame. Figure 4.13 and Figure 4.14 suggest regions of recirculating flow occurred between the wall of the nozzle and the fast-moving central jet, downstream of the nozzle throat. This was also the location of the cavitation front that was not induced by seed particles.

4.3 Particle Image Velocimetry

Particle Image Velocimetry allowed for the measurement of the velocity vector field inside the test section. PIV data was captured at several sections of the nozzle geometry. Independent captures for the converging, diverging, and throat regions of the nozzle were required to produce valid PIV data. The large range of velocities present through the converging-diverging nozzle prohibited a single PIV capture from characterizing the entire nozzle. The converging section of Nozzle-1 was inspected to evaluate the flow profile entering the nozzle throat. The area near the throat and the diverging section immediately following the throat were observed to determine the velocity vector field around the region of cavitation. Areas near the wall, downstream of the throat were observed to examine the details of reversed flow in the nozzle's diverging section.

The PIV measurements presented focus on Nozzle-1, with the upstream reservoir elevated to produce a test section inlet pressure of 104.0 ± 2 kPa. All measurements were taken as close to the maximum flowrate for this nozzle and inlet pressure without initiating cavitation (30 ml/s) with the exception of Figure 4.18, where the PIV measurement was taken just after incipient cavitation with roughly the same flowrate. Figure 4.15 and Figure 4.16 present the averaged PIV flow field over 30 sequential PIV captures; all other PIV measurements were single PIV captures.

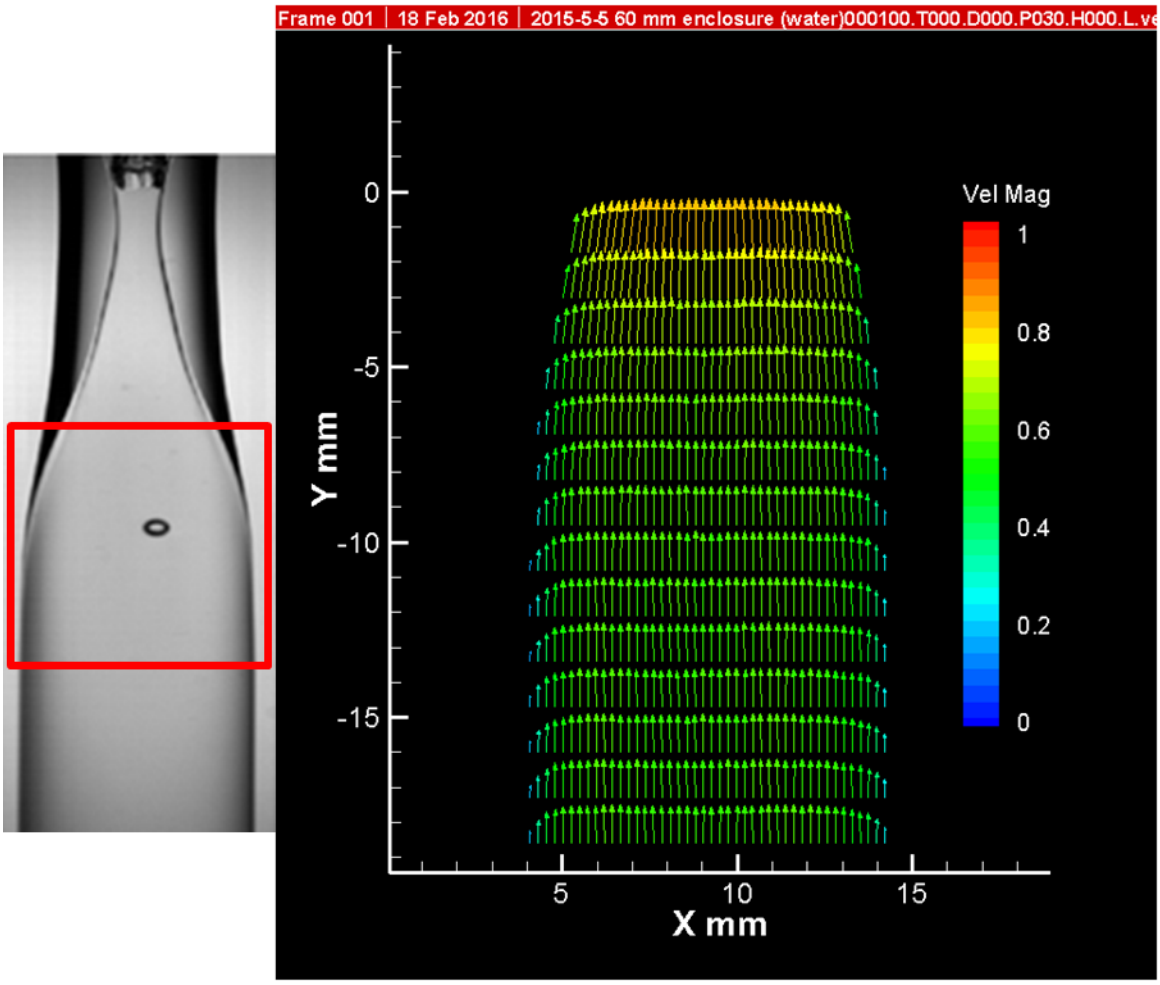

Figure 4.15Nozzle-1 converging section averaged PIV. Velocity magnitude in m/s.

Figure 4.15 shows the averaged velocity vector field for Nozzle-1. The vector field was averaged over 30 PIV captures captured in sequence. The flowrate through the test section was the maximum flowrate dictated by cavitation in the nozzle throat. Figure 4.15 shows that the velocity profile before entering the converging section of the nozzle resembled turbulent flow through a pipe. The velocity rose quickly from no flow at the wall and reached a uniform velocity. The turbulent flow was then accelerated through the converging section leading up to the nozzle throat. Figure 4.15 confirmed that the flow entering the test section was symmetric. The velocity profile remained symmetric as the flow accelerated toward the nozzle throat. The

uniform velocity in the nozzle before the converging section was about 0.5 m/s. This velocity was accelerated to 1.0 m/s at the top of the PIV frame.

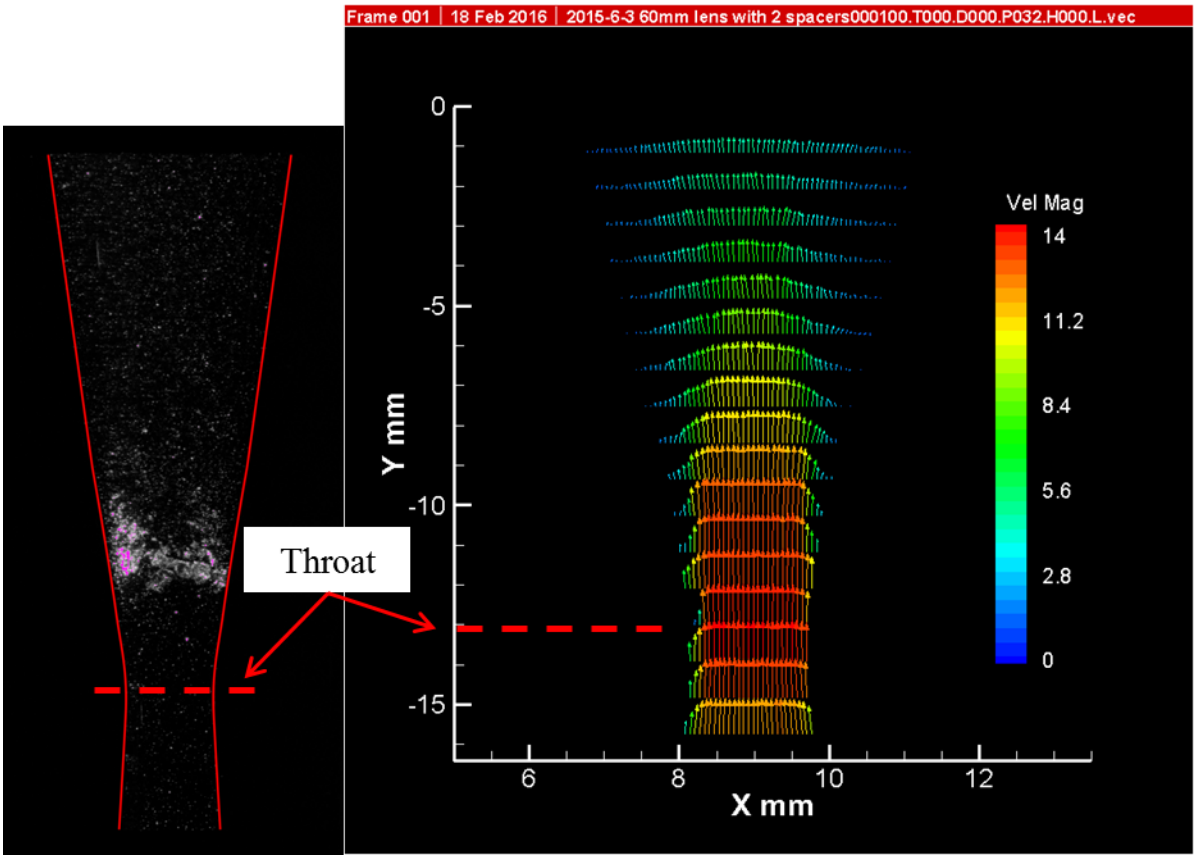

Figure 4.16Averaged PIV capture of Nozzle-1 throat section. Velocity magnitude in m/s.

The flow through the nozzle was accelerated to its maximum velocity through the throat. Figure 4.16 shows the averaged velocity vector field over 30 sequential PIV captures. In Figure 4.16, a maximum velocity of 14 m/s was observed in the nozzle throat. The velocity profile at the throat was similar in shape to the profiles observed in the converging section; the velocity rose quickly from the wall to a uniform profile that spanned almost the entire throat. This near uniform velocity was measured at 14 m/s. The maximum flowrate of about 30 ml/s observed corresponds with an average throat velocity of 14 m/s based on a throat diameter of 1.62 mm. As the flow traveled past the throat, the flow slowed as the nozzle diverged. Past the nozzle

throat, velocity profile also changed. A central jet continued down the center of the nozzle's diverging section. Along the nozzle walls, the flow remained slow in contrast to the central jet.

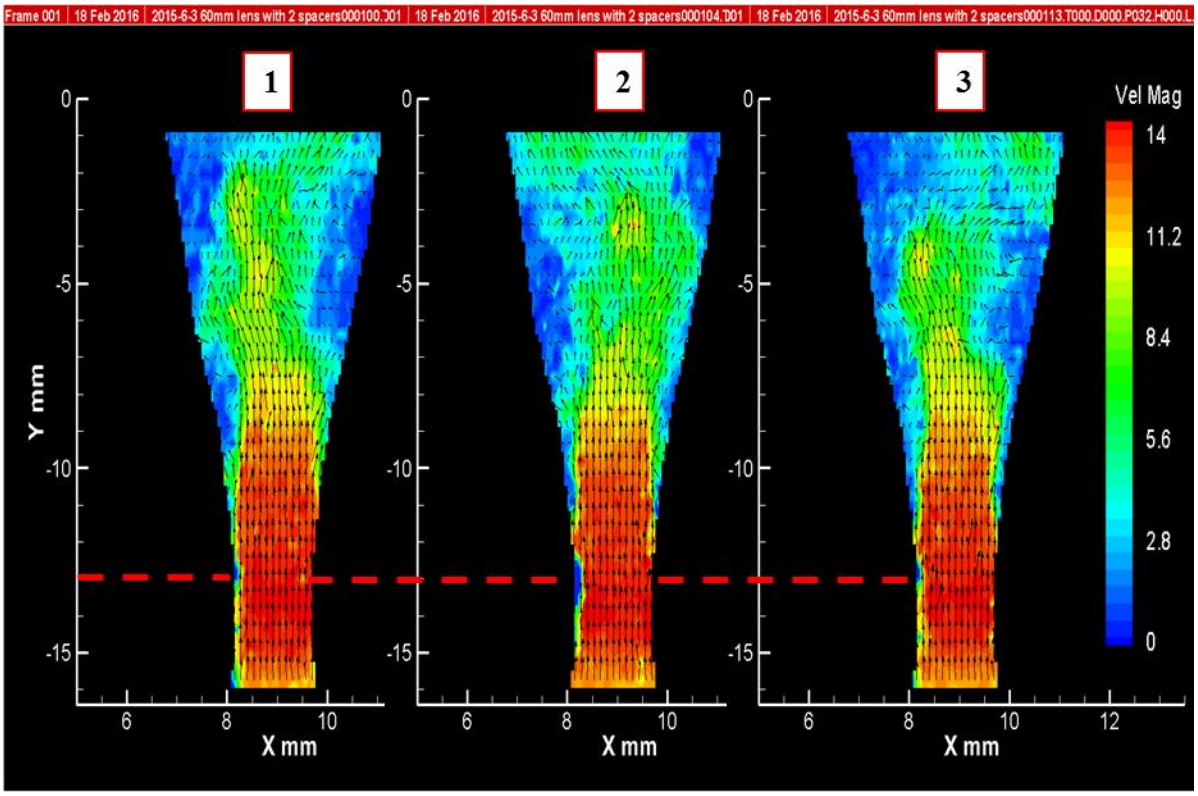

Figure 4.17PIV captures of throat and diverging section of Nozzle-1 with no cavitation. Velocity magnitude in m/s. Throat location indicated with dashed line.

Figure 4.15 and Figure 4.16 illustrated the velocity profile as the flow entered the converging and throat sections. The averaged velocity vector field in Figure 4.16 indicated that the velocity profile changed past the nozzle throat. Figure 4.17 highlights individual PIV captures taken from the same PIV sequence used to compile the average velocity field in Figure 4.16. Figure 4.17 shows that the central flow detached from the nozzle walls, forming a central, wavering jet. The flow around the central jet exhibited low velocity and erratic direction. Figure 4.18 depicts similar conditions that occurred in Figure 4.17 with the exception that cavitation occurred in the PIV captures of Figure 4.18. In Figure 4.18, cavitation occurred approximately 2 mm downstream of the nozzle throat. A raw PIV image from this sequence is shown in Figure

4.16. Cavitation is shown in Figure 4.18 as high velocity flow near a Y position of -12 mm. Note that all PIV coordinates were relative to each PIV measurement's top left location, not representative of a nozzle location. This cavitation prohibited the collection of accurate velocity data. Aside from the regions of cavitation, Figure 4.17 and Figure 4.18 exhibited similar flow patterns in the throat and diverging sections. The maximum velocity observed in the throat for both sequences was 14 m/s. These two figures suggest that flow conditions just before cavitation occurred, and while cavitation occurred, are similar and produce similar flow in the nozzle's diverging section. The low velocity flows around the central jet in both figures exhibit some transient recirculating flow.

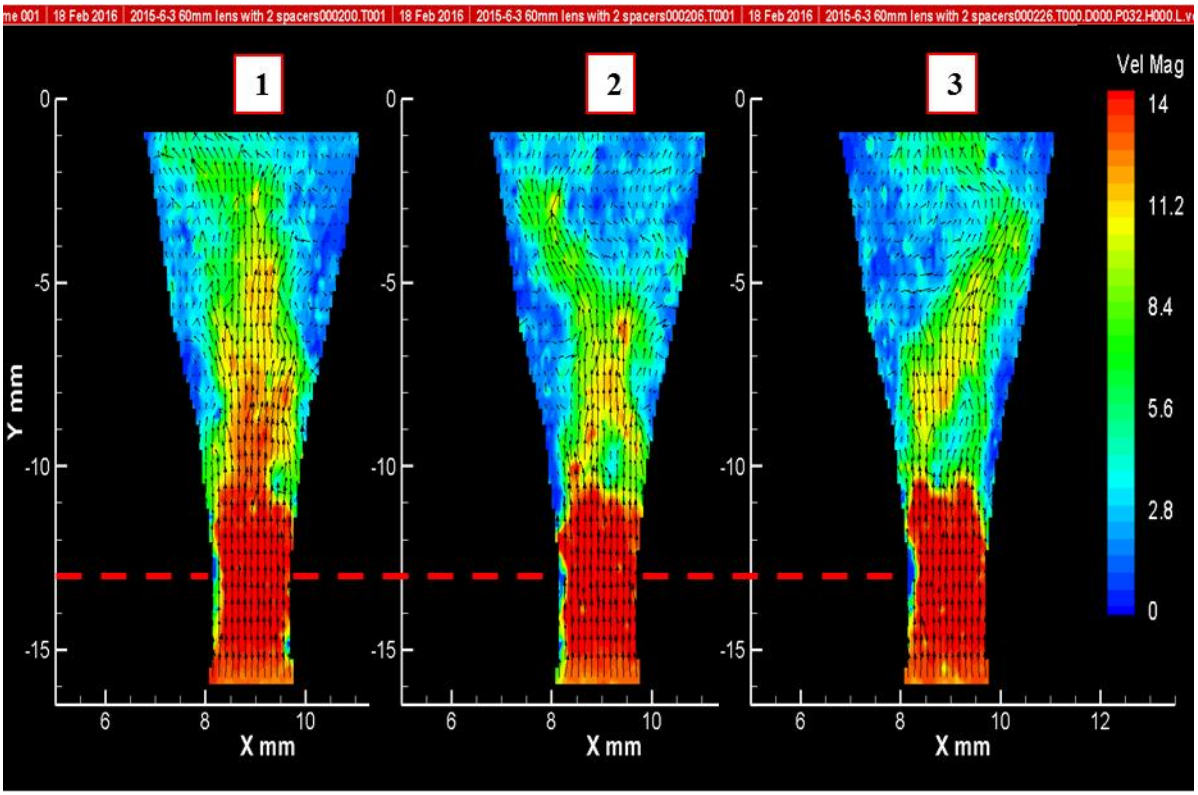

Figure 4.18PIV captures of throat and diverging section of Nozzle-1 with cavitation. Velocity magnitude in m/s. Throat location indicated with dashed line.

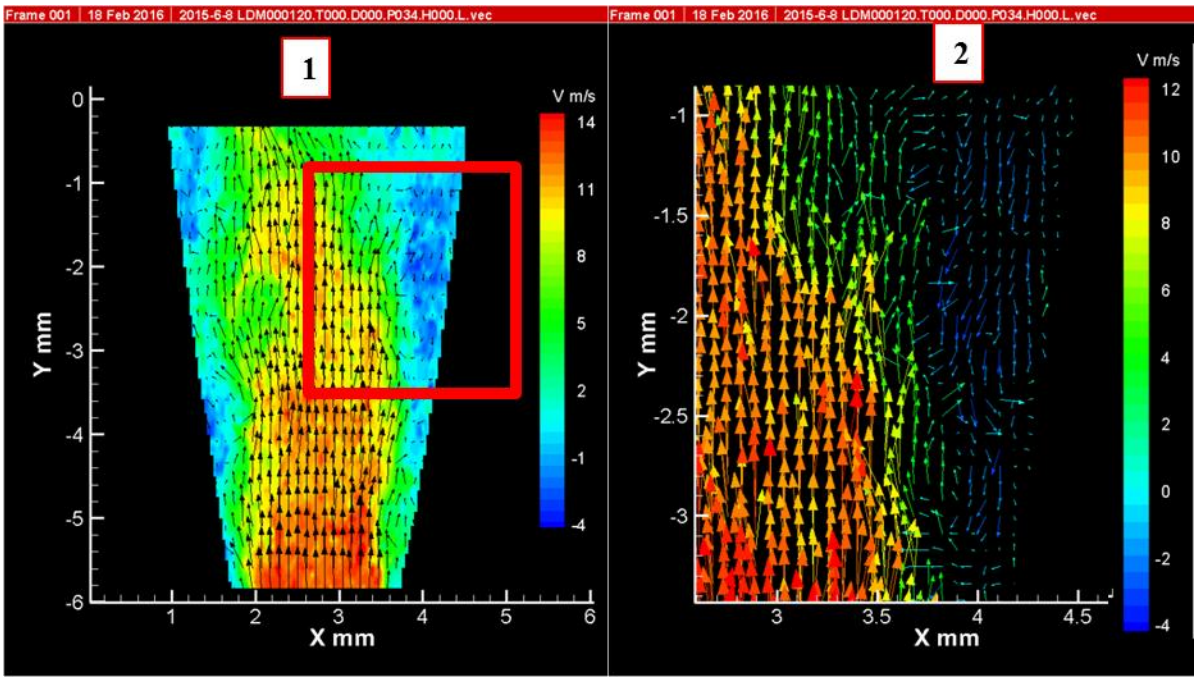

Figure 4.19Detailed view of reversed flow in diverging section of Nozzle-1. Color indicates Y-component of velocity (V) in m/s. Position of frame 2 indicated in frame 1.

The PIV capture shown in Figure 4.19 focused on the slower velocities near the nozzle wall, downstream of the throat. Label 2 in Figure 4.19 shows a detailed view of label 1, where a large velocity gradient occurred between the high velocity, central jet and the reversed flow near the nozzle wall. The color in Figure 4.19 labels the vertical component of each velocity vector generated by the PIV capture. Label 2 displays a large region near the wall that was travelling with a negative vertical velocity as large as 4 m/s. This negative velocity indicated a reversed flow against the flow of the nozzle, and is characteristic of behavior within a separated flow region. The center of Figure 4.19 was approximately 5 mm downstream of Nozzle-1's throat.

The addition of the long-distance microscope allowed for a more detailed analysis of the recirculating region, as indicated in Figure 4.20. The long-distance microscope was connected to the PIV camera and focused on a region near the wall of Nozzle-1 approximately 6 mm downstream of the nozzle throat. The recirculation in this region was large enough to be

captured and the region was far enough downstream from the throat that cavitation would not wash out the view of the camera.

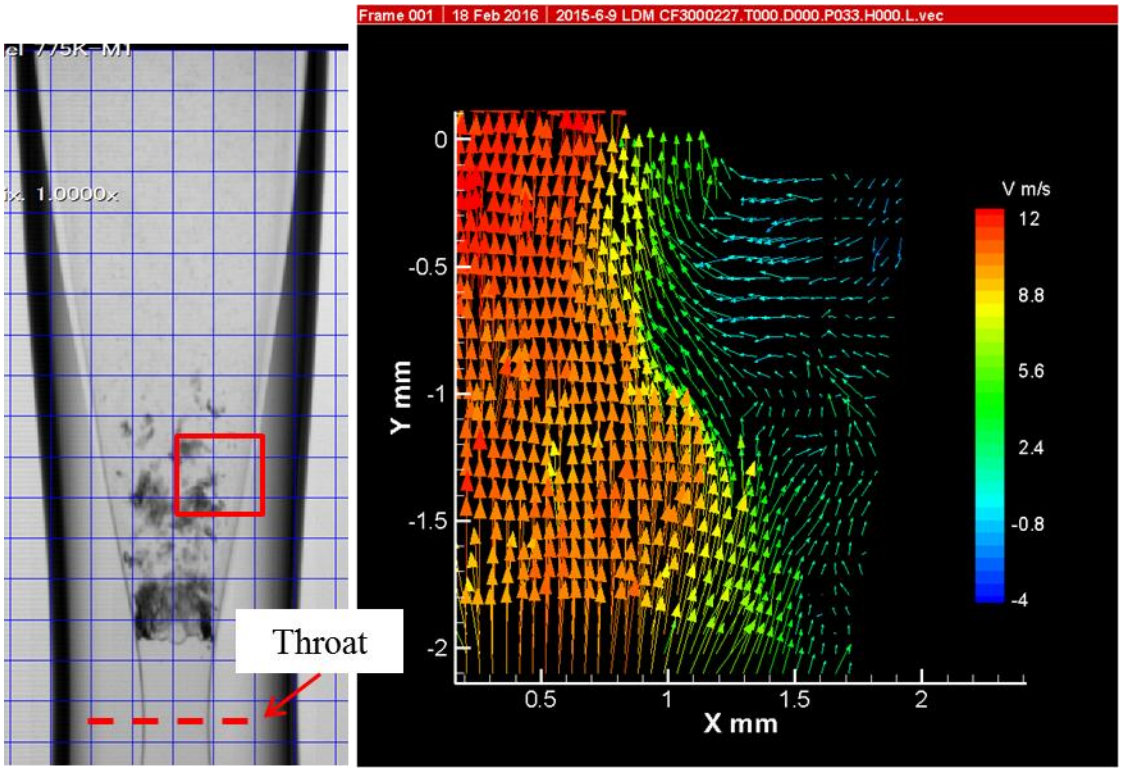

Figure 4.20PIV capture near wall of diverging section of Nozzle-1. Color indicates Y-component of velocity in m/s. Location indicated relative to throat. Grid size of 1.0 mm.

Figure 4.21 displays two PIV captures from the same region as Figure 4.20. In Figure 4.21, label 1 presents a large region along the wall that was flowing against the flow of the nozzle with a vertical velocity of -3.5 m/s. Label 2 in Figure 4.21 shows the formation of a vortex between the central jet, which travelled upward, and flow near the wall, which travelled downward. This vortex was able to produce downward velocities of -4.5 m/s.

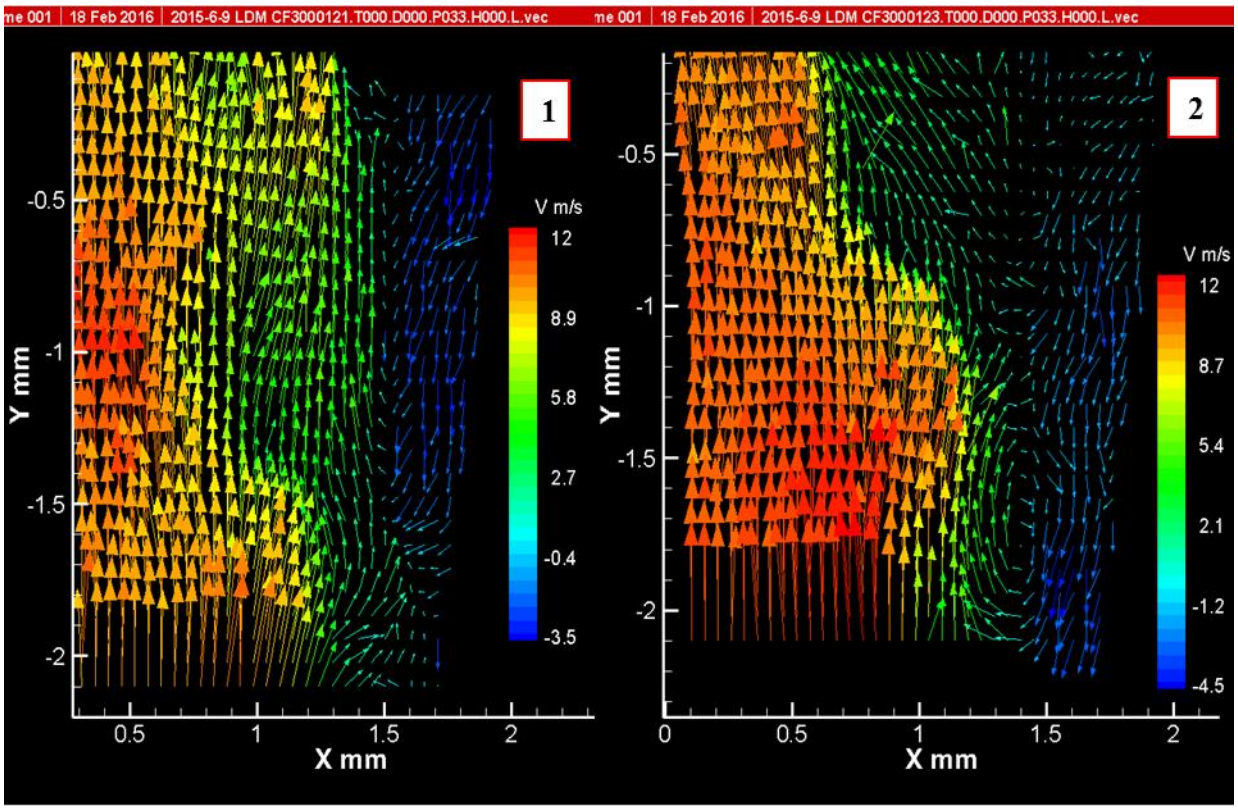

Figure 4.21PIV captures near wall in Nozzle-1. Location indicated in Figure 4.20. Color indicates Y-component of velocity in m/s.

The reversed flow near the nozzle wall in the diverging section detailed in Figure 4.20 and Figure 4.21 demonstrated that the flow upward through the nozzle detached from the wall at some point downstream from the nozzle throat. Figure 4.17 and Figure 4.18 indicated that regions of low velocity and reversed flow persisted as close as 3 mm downstream from the nozzle throat. Figure 4.18 has shown that this region of recirculation was close to the onset of cavitation, around 2 mm downstream from the nozzle throat. The low pressures in this region put the water flow at risk of cavitation. The presented examples of large eddy formation just downstream of the nozzle throat provided more incentive for the flow to cavitate.

Chapter 5 - CFD Simulations

A series of computation fluid dynamic (CFD) models were developed alongside the experimental work detailed in chapters three and four. ANSYS Fluent was used to simulate the water flow through Nozzle-1. The model mesh was generated using ANSYS ICEM. Several mesh models were created as the CFD model was refined. This chapter presents results from the best model obtained to date.Software information presented in Appendix D. Convergence for each particular model was based on the continuity, velocity, and turbulence source term scaled residuals reported by Fluent. For convergence, each scaled residual must have decreased below a threshold (dependent on turbulence model) and remained there for at least 50 time steps.

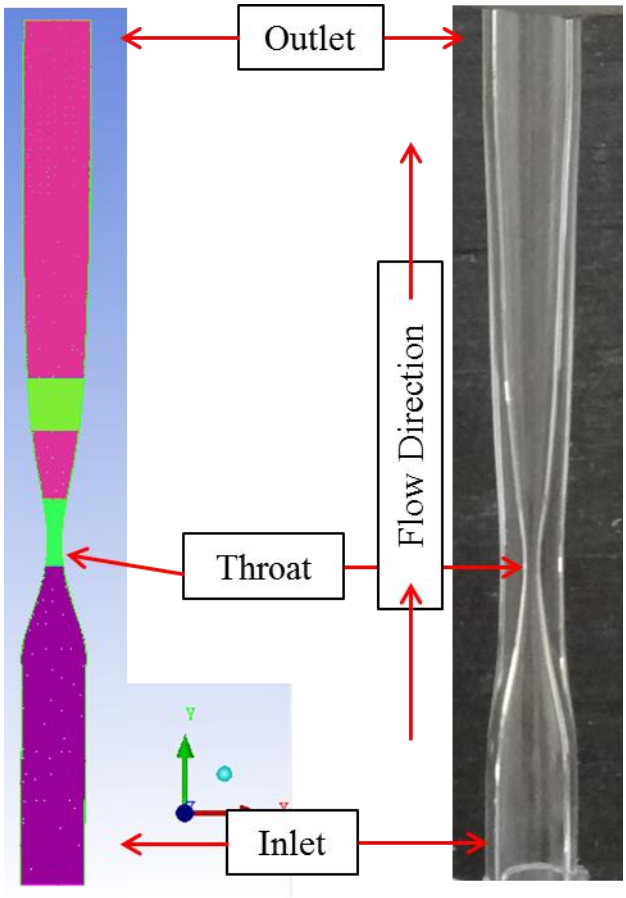

Figure 5.1 CFD model mesh (left) shown with corresponding real nozzle (right) in vertical orientation. Mesh zones shown in separate colors.

5.1 Model Mesh

Several iterations of mesh models were created in an attempt to better model the water flow through Nozzle-1. Figure 5.1 shows the best performing mesh model. A digital photo of Nozzle-1 was used to determine the shape of the interior nozzle wall, much like the plot shown in Figure 2.2. The nozzle profile data was used to recreate the nozzle wall in the meshing software, ICEM. A straight region was added upstream of the nozzle converging section to allow the flow to more fully develop from the inlet boundary, shown as the nozzle inlet at the bottom of Figure 5.1. Similarly, a straight section was added downstream from the diverging section so the model would better capture the flow behavior in the diverging section.

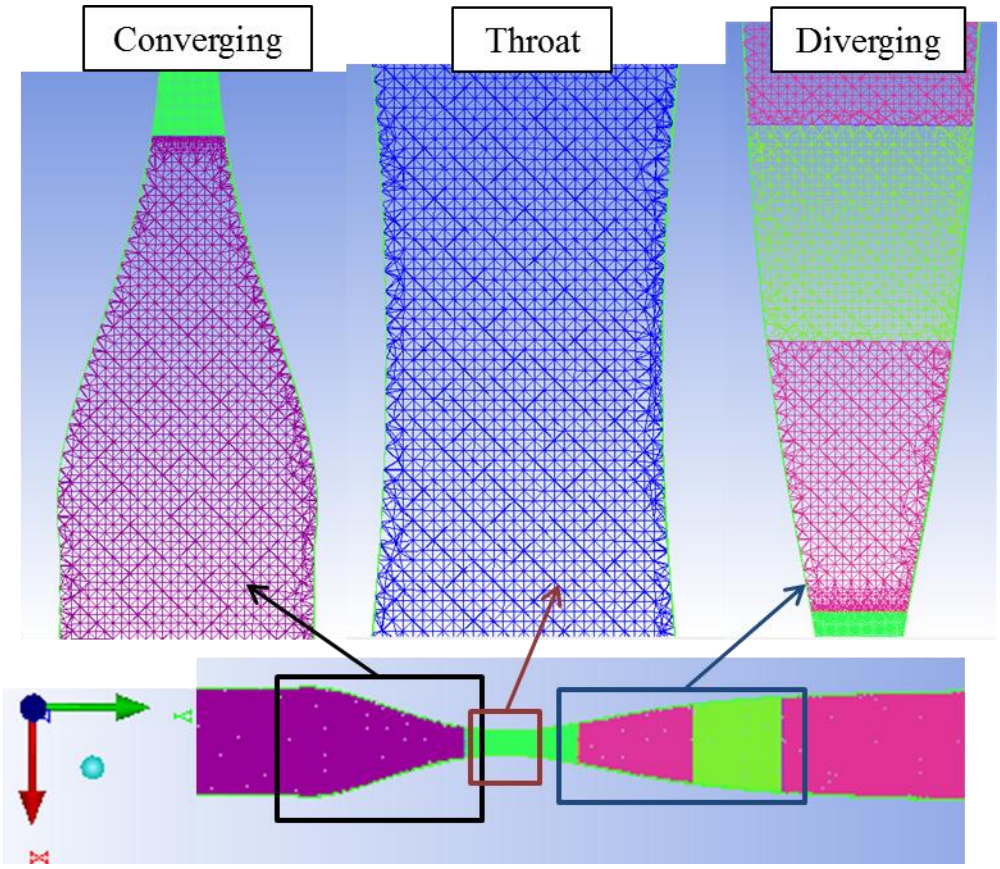

Figure 5.2 CFD model mesh detail of Nozzle-1's converging, throat, and diverging sections. Converging and diverging sections shown on same scale, throat section enlarged. Model contained 617,000 elements.

After the geometry of Nozzle-1 was created, the geometry was split into several sections, shown in different colors in Figure 5.2. These sections were used to control the mesh density in different sections of the nozzle. Figure 5.2 demonstrates the different mesh densities used in the model. A more course mesh was used in the nozzle inlet and converging regions (0.8 mm element size). The region near and just past the nozzle throat necessitated a fine mesh, due to the high fluid acceleration and the decreased physical size of the nozzle throat compared to the inlet regions. This section near the throat, shown enlarged in Figure 5.2, carried the smallest mesh element size of 0.1 mm. The mesh density in the nozzle's diverging section was also increased to capture the flow characteristics of the water jet leaving the nozzle throat. The model mesh, presented in Figure 5.2, was irregular near the nozzle wall; this irregularity was due to the internal structure of the model mesh, which was based on Cartesian coordinates. Where the regular, internal mesh structure met the surface mesh on nozzle wall, the meshing software automatically connected the internal and surface meshes. Additionally, when the meshing software smoothed the mesh, the internal mesh nodes greatly outnumbered the surface mesh nodes; therefore, the smoothing operation favored smoothing the model mesh internal structure more than smoothing the interface of the internal mesh and the surface mesh. The CFD model that used these previously discussed mesh densities provided smooth results without large discontinuous regions and was not computationally prohibitive. It contained 617 thousand elements (k elements). Models with less mesh elements, 287 and 297 k elements, produced discontinuities near the throat and other near-wall locations due to relatively large element sizing. Another model with 878 k elements performed similarly to the 617 k element model discussed throughout most of this chapter. Larger models with up to 1.37 million elements were

simulated and found to be extremely computationally expensive and performed similarly to the 617 k element model.

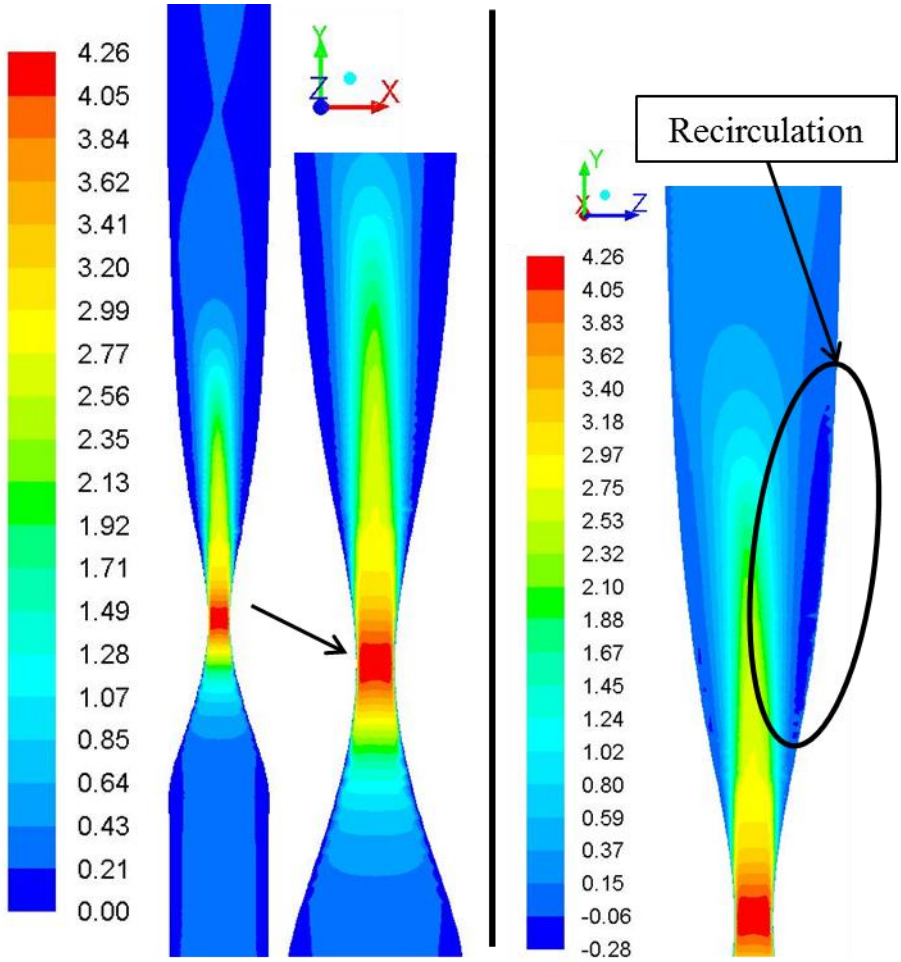

Figure 5.3 CFD k-ε model velocity magnitude (left) and vertical velocity (right) contour plots with uniform inlet velocity of 0.2 m/s. Velocities plotted in m/s.

5.2 Low Velocity Model

After the appropriate model mesh was created, several different CFD models were used to simulate the water flow through Nozzle-1. Figure 5.3 shows the velocity contour plot of Nozzle-1's mid-plane for a uniform inlet velocity of 0.2 m/s. For simplicity, a uniform inlet velocity was chosen for the inlet boundary condition, which produced a similar velocity profile, shown in Figure 5.4, tothe velocity profile observed immediately prior to Nozzle-1's converging

section, presented in Figure 4.15. A realizable k-epsilon turbulence model was used to model the viscous effects in the simulation. Figure 5.3 shows the flow velocity increased to a maximum velocity of 4.26 m/s at the nozzle throat. The contour plot also shows a high-velocity central jet formed in the center of the diverging section, similar to the central jet seen in Figure 4.16. The contour plot of the vertical velocity, presented in Figure 5.3, also exhibits a small area of recirculated flow near the wall in the diverging section.

The velocity profile at several axial locations of the model were compared with PIV measurements in Figure 4.16. Figure 5.5 shows the axial component of the velocity normalize to the average axial throat velocity of the CFD model with an inlet velocity of 0.2 m/s. The radial position was normalized with the model throat radius. All of the profiles agree with PIV measurements shown in Figure 4.16. A fully developed turbulent velocity profile at the nozzle throat (0.0mm) diffused into a central jet and flattened in the diverging section (30.0 mm downstream from throat).

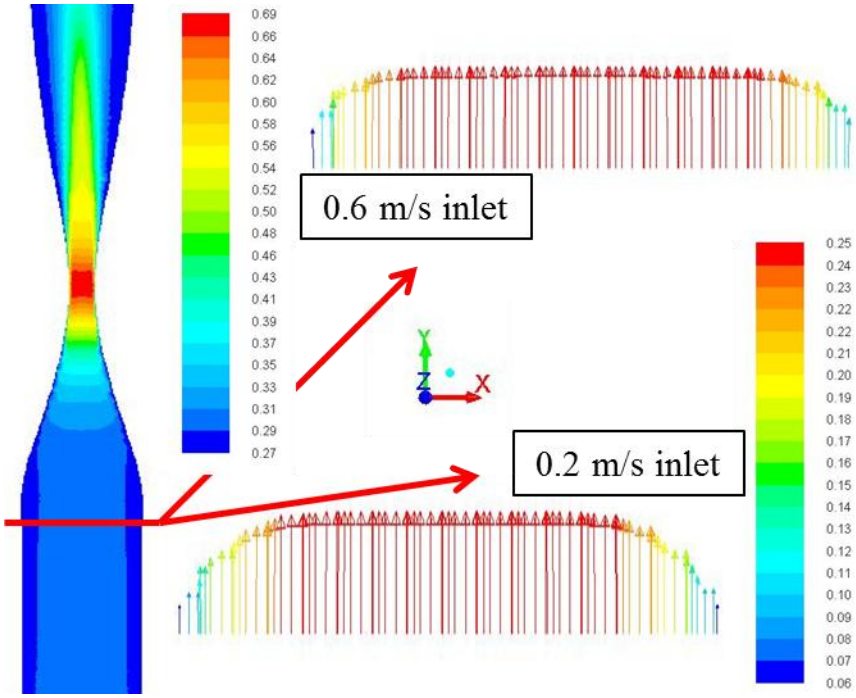

Figure 5.4 Inlet section velocity profile for inlet velocities of 0.2 m/s (bottom) and 0.6 m/s (top).

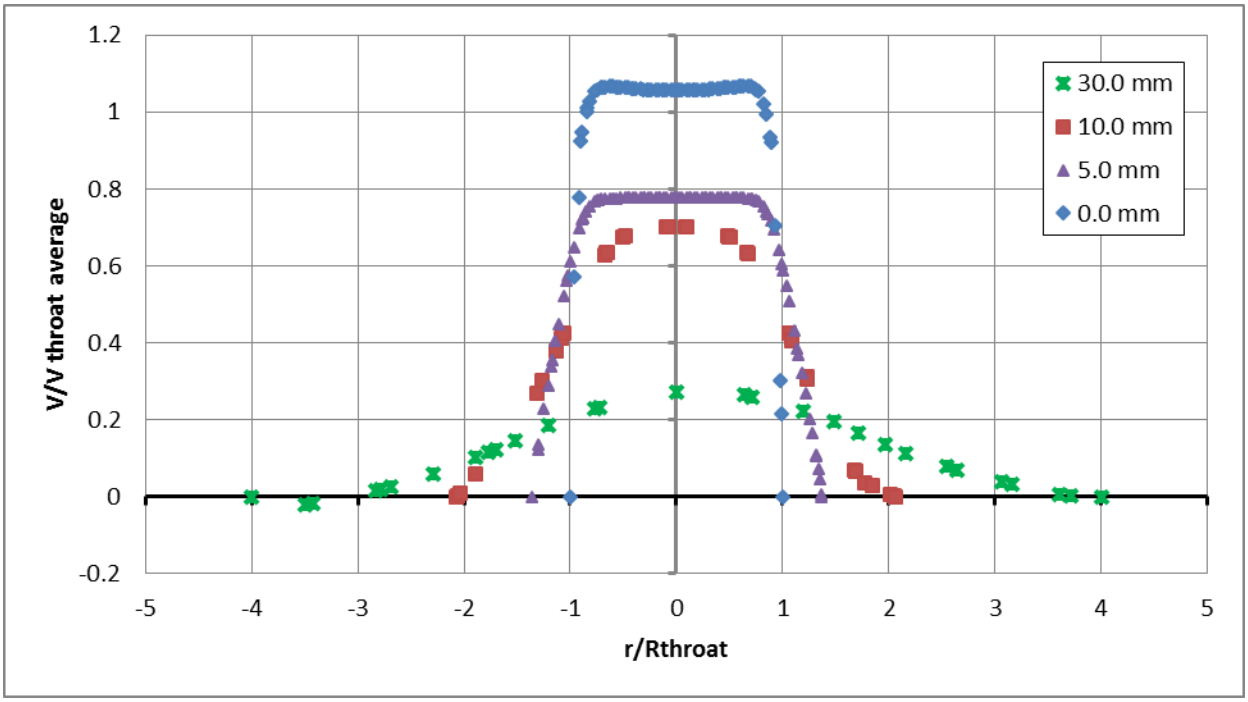

Figure 5.5CFD normalized axial velocity vs normalized radial position for several positions at and downstream of nozzle throat for inlet velocity of 0.2 m/s.

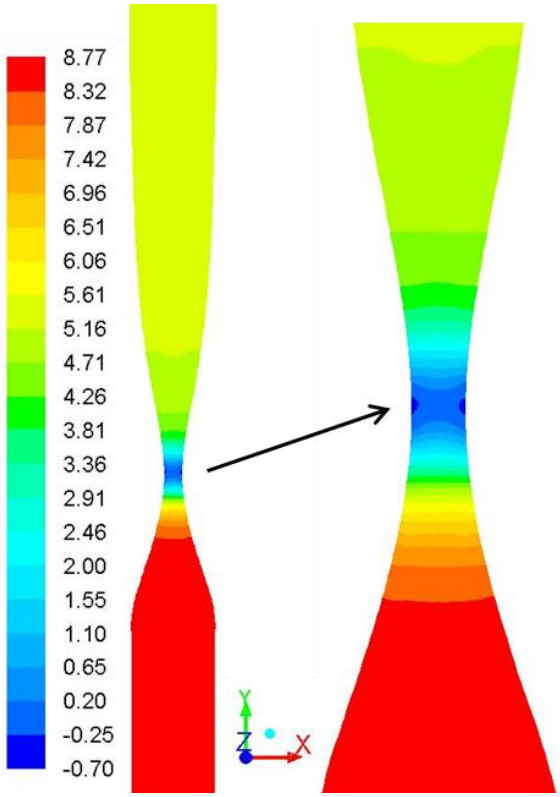

Figure 5.6 CFD model static pressure (kPa) contour plot for inlet velocity of 0.2 m/s.

The static pressure of the model was set to an initial reference value of zero Pascals at the nozzle inlet boundary.Figure 5.6 shows the final static pressure contour plot. The pressures presented in Figure 5.6 are somewhat analogous to a gauge pressure required to drive the flow at the prescribed inlet velocity of 0.2 m/s. The CFD model predicts a throat pressure of 9.5 kPa below inlet pressure and a pressure drop from the nozzle inlet to outlet of 3.2 kPa. The minimum pressure in the nozzle, emphasized in Figure 5.6, occurred in the nozzle throat at the wall. If the pressure minimum occurred at this location in Nozzle-1, cavitation would be expected to initiate at the wall in the nozzle throat.

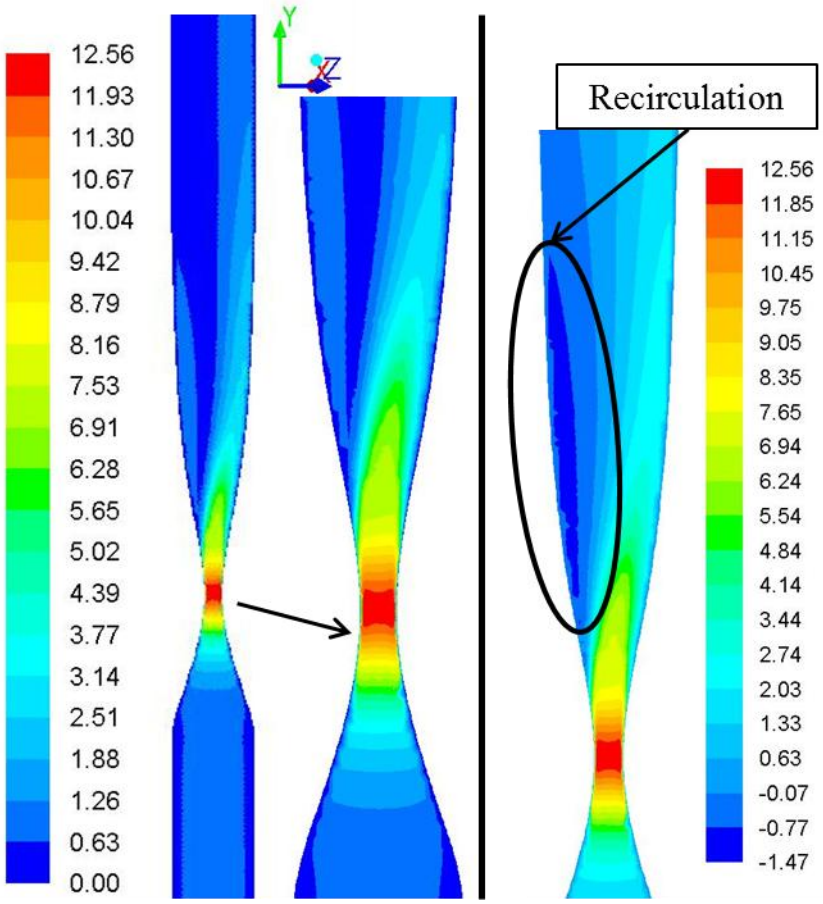

Figure 5.7 CFD k-ε model velocity magnitude (left) and vertical velocity (right) contour plots with uniform inlet velocity of 0.6 m/s. Velocities plotted in m/s.

5.3 High Velocity Model

The CFD model discussed in section 5.2 was stable for inlet velocities up to 0.2 m/s, which generated a modest 4.26 m/s velocity at the throat, well below throat velocities measured by PIV or based on measured flowrate (rotameter). When the model inlet velocity was increased to produce higher throat velocities, the jet in the nozzle's diverging section attached to the nozzle wall. Once the jet established a location on the nozzle wall, it remained steady, as shown in Figure 5.7. The steady jet observed in the model's diverging section does not agree with the transient jet seen in Figure 4.17. At moderate to high velocities, the CFD model does not agree with the PIV measurements. The CFD model did develop a large recirculation region in the

nozzle's diverging section, shown in Figure 5.7. This large recirculation flow pattern was also seen in PIV measurements, albeit in a transient form. As with an inlet velocity of 0.2 m/s, the flow was sufficiently developed before entering the nozzle's converging section, shown in Figure 5.4.

The velocity profiles at several axial locations in the high velocity CFD model and compared with PIV measurements. Figure 5.8 shows the axial velocity data taken from the CFD model. The velocity profile at the throat (0.0 mm) was very flat. The profile started to show asymmetry at 5.0 mm. Some reversed flow was seen at 10.0 mm downstream from the throat. At 30.0 mm downstream, a large portion of the flow had reverse. This behavior was not consistent with the averaged PIV measurements shown in Figure 4.16.

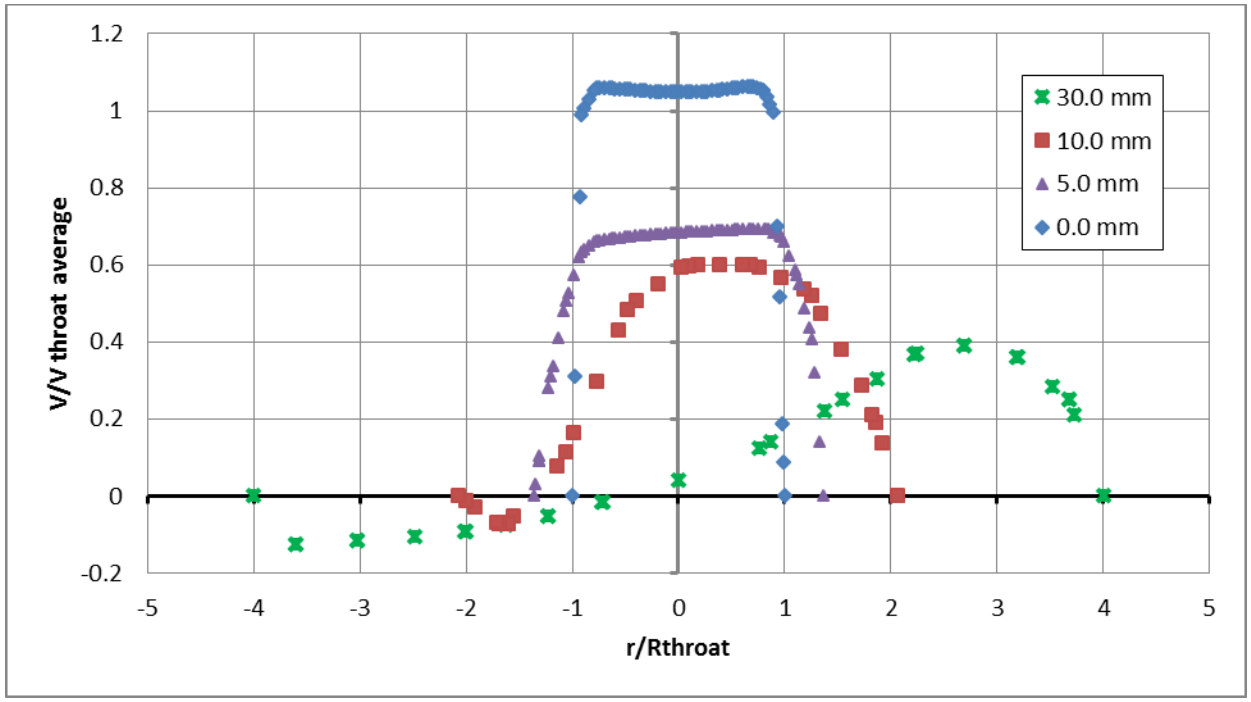

Figure 5.8 CFD normalized axial velocity vs normalized radial position for several positions at and downstream of nozzle throat for inlet velocity of 0.6 m/s.

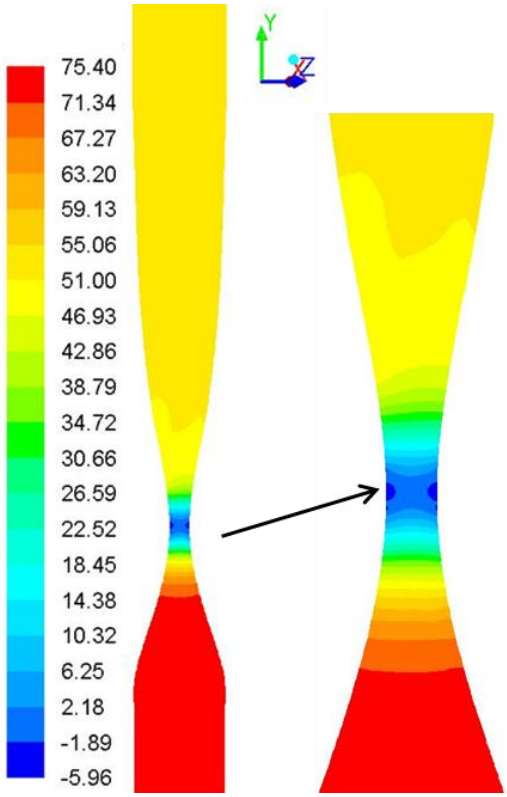

Figure 5.9CFD model static pressure (kPa) contour plot for inlet velocity of 0.6 m/s.

Figure 5.9 shows the pressure distribution from the k-epsilon turbulence model for a nozzle inlet velocity of 0.6 m/s. The same reference pressure of zero pascals was used for both Figure 5.6 and Figure 5.9. As before, the minimum static pressure was located in the nozzle throat at the wall. A larger pressure gradient was required to achieve an inlet velocity of 0.6 m/s;the pressure at the throat was depressed 81 kPa below the inlet pressure, with a pressure drop from the inlet to the nozzle outlet of 21.5 kPa. As with Figure 5.6, Figure 5.9 does not show a large pressure variation at each axial position of the nozzle, except near the throat.

5.4 Other Viscous Models

Several other viscous models were applied to Nozzle-1's mesh model. The first and most simple model was laminar flow. This model failed to converge, as even low inlet velocities lead to turbulent flows within the nozzle throat. Next, the standard k-epsilon turbulence model was

applied to the model. K-epsilon converged to a solution and produced reasonable velocity contour plots, leading to the use of the realizable k-epsilon model presented in this chapter. Additionally, the k-omega model was tested. This model failed to converge to a solution. The Reynolds Stress model was extremely computationally expensive and failed to converge to a solution.

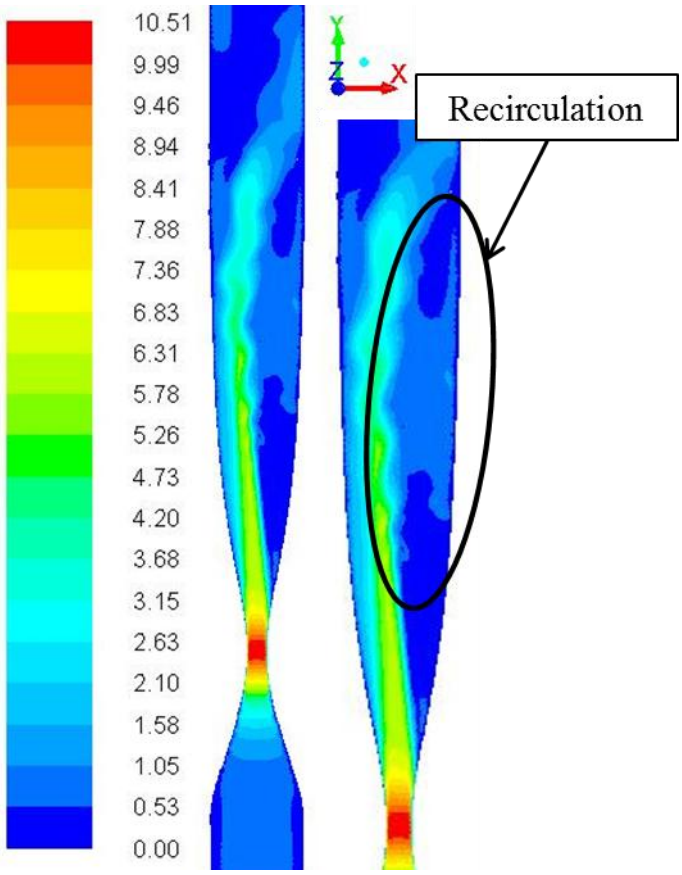

Figure 5.10 CFD detached eddy simulation (DES) model velocity magnitude (m/s) contour plot with uniform inlet velocity of 0.5 m/s.

Large eddy simulation (LES) and detached eddy simulation (DES) were also applied to Nozzle-1's model. Both were computationally more expensive than the k-epsilon model. DES provided similar results as the k-epsilon model at velocities greater than 0.2 m/s, presented in Figure 5.10. As with the k-epsilon model, DES favors a particular wall in the nozzle's diverging

section and remains near that wall. DES also produced a large recirculation region on the nozzle wall opposite the attached jet, similar behavior to the k-epsilon model.

Chapter 6 - Conclusions and Recommendations

6.1 Summary and Conclusions

Flow characteristics of the constructed flow system were studied. The test section inlet and outlet pressures controlled flow through the system. Volumetric flowrate measurements were taken for a range of pressures across the system test section. Pressure measurements were made of the test section inlet and outlet for a range of volumetric flowrates with and without cavitation. Velocity measurements were taken of injected bubbles and seed particles as they traveled through the test section. A high-speed digital camera was used to visualize the flow within the test section and the flow characteristics of cavitation. Particle Image Velocimetry (PIV) measurements of the velocity field were taken of the entire test section and in more detail at specific locations within the test section. A computation fluid dynamics (CFD) model was developed to model water flow in Nozzle-1. Velocity data from the model was compared to PIV measurements. Pressure data from the CFD model was examined and compared to pressure measurements at the test section inlet and outlet.

The first evidence of choked flow was found while measuring the water flowrate while controlling the test section inlet and outlet pressures. For two independent test section inlet pressures, the test section outlet pressure was regulated through a range of decreasing back pressures. The flowrate through the test section increased as the outlet pressure dropped until a maximum flowrate for each inlet pressure was reached. After the maximum flowrate was achieved, the flow behaved similar to choked gas flow through a converging nozzle; the flowrate remained constant as the outlet pressure was continually reduced. This choked condition always coincided with the onset of cavitation. This behavior suggested the flow was reaching a sonic condition at some point within the nozzle. When the maximum flowrate was approached slowly,

flowrates slightly higher than the maximum flowrate could be briefly attained until cavitation initiated and the flowrate would snap back down to the established maximum flowrate. This behavior suggests a metastable liquid state was reached within the nozzle before the onset of cavitation. Pressure data gathered at the test section outlet supported the choked flow behavior; the outlet pressure dropped alongside the vacuum chamber pressure while the test section inlet and flowrate remained choked. All of these behaviors were observed in both Nozze-1 and Nozzle-2.

A high-speed digital camera was used to visualize the flow patterns and location of the onset of cavitation in both nozzles. High-speed video was used to track both seed particles and bubbles to indirectly measure velocity as water flowed through the converging section of Nozzle-1. These measurements up to the nozzle throat agreed with averaged velocities based on the measured flowrate. High-speed video captured both the transient onset of cavitation and the steadier established cavitation flow patterns. Cavitation was observed with different levels of dissolved gasses present in the water. It was found that removing the dissolved gasses did not affect the cavitation structure or onset in the nozzle. High-speed video was also used to determine the effect of introducing seed particles to the flow in the form of 10 μm and 120 μm hollow glass spheres. Only the 120 μm seed particles affected cavitation formation and provided nucleation sites for cavitation to form at the nozzle throat, upstream from the cavitation onset location. The seed particles were tracked using high-speed video without cavitation occurring and revealed regions of separated and recirculating flow in the diverging region of the nozzles, immediately following the throat.

PIV was used to gather the velocity vector field data from all sections Nozzle-1 and Nozzle-2. The inlet section of each nozzle demonstrated the velocity profile entering the

converging section resembled fully developed turbulent flow. This profile was accelerated through the nozzle throat and formed a transient central jet through the diverging section. The areas of recirculation near the nozzle wall in the diverging sections were interrogated to determine how much recirculation occurred in the diverging section. PIV showed that the recirculation can be as fast as 4.5 m/s against the nozzle bulk flow (i.e., reversed flow). PIV showed the areas of recirculation also coincide with the cavitation front, approximately 2 mm downstream of the throat. Throat velocities measured with PIV also agreed with the averaged velocities based on flowrate measurements.

A (CFD) model was developed using the commercially available software ANSYS Fluent. The velocity distribution was compared to the previously gathered PIV measurements. The velocity field produced by the k-epsilon model at very low flow conditions had the same shape as the averaged PIV velocity field. Laminar, k-epsilon, k-omega, Reynolds stress, large eddy simulation, and detached eddy simulation viscous models failed to reproduce expectedvelocity field results in the realm of velocities observed in the real-world counterpart of the model. Each model either was unable to converge to a solution of the flow in the diverging section, or it attached to a particular wall location and stayed there. The low flow models were able to reproduce similar inlet velocity profilesto the nozzle converging section as those observed with PIV. The pressure data generated by the CFD models indicated the minimum pressure was in the throat on the nozzle wall. This did not seem reasonable considering where the onset of cavitation has been observed. The k-epsilon, large eddy simulation, and detached eddy simulation viscosity models did create a recirculation region on the wall opposite of the attached flow.

6.2 Recommendations for Future Work

It appears that the flow separation from the diverging nozzle wall coincides with the formation of cavitation. The nozzle could be redesigned in an attempt to delay or prevent this separation. The characteristics of diffusers have been studied in the past and these studies may provide insight to any design changes to the nozzle geometry to avoid flow detachment from the nozzle wall. The use of vanes in the diverging section could promote wall attachment, or the design of an annular diffuser with more control over the manufactured shape of the nozzle. The flow characteristics demonstrated by Nozzle-1 and Nozzle-2 suggest that the areas immediately following the nozzle throat are critical in determining flow attachment. Change to this area of the nozzle should be considered next.

The lack of pressure data inside the nozzle limits our understanding of the conditions leading to cavitation formation. Gathering this pressure data also presents a significant problem, due to the small size of the nozzle and the flow's sensitivity to nucleation. A simple pressure tap could promote cavitation in a completely new location.

Work on a reliable CFD model should be a high priority. Any model, even if limited, would provide a significant design insight and direction for real-world improvements on delaying cavitation formation. The next challenge in developing a meaningful CFD model is the production of a properly distributed mesh. Without a mesh that is densely and regularly populated in the areas of the nozzle that poses large velocity and pressure gradients, the viscous and cavitation models are irrelevant.

References

[1] J.-P. Franc, "Physics and control of cavitation," *Design and Anal. High Speed Pumps*, pp. 2.1-2.36, Mar. 2006.

[2] M. P. Davis, "Experimental investigation of the cavitation of aviation fuel in a converging-diverging nozzle," Ph.D. dissertation, Dept. Aerospace and Mech. Eng., Univ. of Notre Dame, Notre Dame, IN, 2008.

[3] P. Rudolf, M. Hudec, M. Gríger and D. Štefan, "Characterization of the cavitating flow in converging-diverging nozzle," *EPJ Web of Conf.*, vol. 67, p. 02101, Mar. 2014.

[4] K. Schaber and G. H. Schnerr, "M11 Spontaneous condensation and cavitation," *VDI-Buch, VDI Heat Atlas*, pp. 1391-1420, 2010.

[5] A. Sou, S. Hosokawa and A. Tomiyama, "Effects of cavitation in a nozzle on liquid jet atomization," *Int. J. Heat and Mass Transfer*, vol. 50, no. 17-18, pp. 3575-3582, Aug. 2007.

[6] G. B. Wallis, One-dimensional two-phase flow, New York: McGraw-Hill, 1969.

[7] J. P. Franc and J. M. Michel, Fundamentals of cavitation, Dordrecht, Netherlands: Kluwer Academic Publishers, 2004.

[8] F. Caupin, "Escaping the no man's land: Recent experiments on metastable liquid water," *J. Non-Crystalline Solids*, vol. 407, pp. 441-448, Jan. 2015.

[9] E. Goncalves and R. F. Patella, "Numerical simulation of cavitating flows with homogeneous models," *Comput. and Fluids*, vol. 38, no. 9, pp. 1682-1696, Oct. 2009.

[10] M. Yang, S. Xiao, C. Kang and Y. Wang, "Effect of geometrical parameters on submerged cavitation jet discharged from profiled central-body nozzle," *Chinese J. Mech. Eng.*, vol. 26, no. 3, pp. 476-482, 2013.

[11] H. Huang, D. Dabiri and M. Gharib, "On errors of digital particl image velocimetry," *Measurement Sci. Technology*, vol. 8, no. 12, pp. 1427-1440, Dec. 1997.

[12] J. Wilms, "Flow visualization of cavitation," M.S. thesis, Dept. Mech. and Nucl. Eng., Kansas State Univ., Manhattan, 2013.

Appendix A - PIV Equipment Specifications

This appendix describes the particular Particle Image Velocimetry (PIV) equipment used to gather the PIV data presented in this thesis. See Appendix D for a description of the software used in conjunction with the PIV equipment. Figure 2.4 shows the setup of the PIV equipment.

The uncertainty of PIV measurement techniques was studied by Huang [11]. Huang found the RMS and mean-bias errors were on the order of 0.1 pixel. Typical PIV measurements taken of the test section used a rectangular interrogation gird and were approximately 100 pixels long (axial direction). A mean particle displacement of 10 pixels was assumed. This would cause roughly a 1% error in displacement measurements. The timing setup has a fraction of this error, estimated at <0.1%; therefore, the calculation of particle displacement was the main source of error. The total error of any one velocity vector would be on the order of 1%, and likely less than 2% of the measured velocity.

Camera

- POWERVIEW Plus 4MP (megapixel)
- Model: 630159

Figure A.1 PIV camera shown with 60 mm lens.

Dual Nd:YAG Lasers

- YAG New Wave
- Manufacturer: New Wave Research
- Model: Gemini-15Hz

Figure A.2 Nd:YAG laser.

Synchronizer

- 610036 LaserPulse Synchronizer

Figure A.3 PIV synchronizer.

Frame Grabber

- Xcelera-CL PX4

Appendix B - High-Speed Digital Camera Specifications

The high-speed digital camera used to capture high-speed video and pictures was a Photron FASTCAM SA5 model 775K-M1.Table B.1 details the specifications of the particular camera used.Figure 2.5 shows the setup used for the high-speed camera.

Image Sensor	CMOS image sensor	
Sensor Resolution	1,024 x 1,024 pixels	
Frame Rate	When full frame: 7,000fps max. When a frame segment: 775,000 fps max.	
Lens Mount	F mount, C mount, Lens Mount with Filter Changer (optional)	
Recording Color Depth	Monochrome	12bit
	Color	RGB, each 12-bit (Bayer color filter method)
Shutter Method	Electronic shutter	
Recording Method	IC memory	
Recording Memory Capacity	8 GB (model 1), 16 GB (model 2), 32 GB (model 3)	
Trigger Method	START, CENTER, END, MANUAL, RANDOM, RANDOM RESET, RANDOM CENTER, RANDOM MANUAL, TWO STAGE	
Gain Control	Hardware LUT on camera Controllable via LCD Remote Controller or software	
Image Output Customization	Customizable LUT, brightness is changeable	
External Synchronization Input Signal	5 Vp-p, negative polarity/positive polarity (switchable)	
External Synchronization Output Signal	5 Vp-p, negative polarity/positive polarity (switchable)	
Trigger Input Signal	TTL, contact	
Other Output Signals	Other timing signal outputs, event marker input	
External Control	LCD Remote Controller, RS-422 external control I/F, Gigabit Ethernet I/F (PC)	
Video Output Signal	NTSC/PAL, HD SDI (Compliant with SMPTE 292M 1,080i) -59.94/60Hz Selectable (NTSC mode) -50Hz (PAL mode) With digital zoom, scroll, fit functions	
Digital Interface	Gigabit Ether (1000BASE-T)	

Table B.1High-speed digital camera model specifications.

Table B.2 describes the memory limits of the high-speed camera used. For specific resolutions, Table B.2enumerates the maximum framerate, recording time, and number of

frames. The resolution of the high-speed camera was adjustable any resolution smaller than 1024 x 1024 pixels.

Resolution	Max Framerate	8G Model Rec Times	8G Model Rec. Frames
1,024 × 1,024	7,000	0.780	5,457
1,024 × 1,000	7,500	0.745	5,588
1,024 × 888	8,400	0.749	6,293
1,024 × 800	9,300	0.751	6,985
1,024 × 752	9,300	0.799	7,431
1,024 × 640	10,000	0.873	8,731
1,024 × 512	14,000	0.780	10,914
896 × 896	9,300	0.766	7,127
896 × 848	10,000	0.753	7,531
896 × 704	12,000	0.756	9,071
768 × 768	12,500	0.776	9,701
768 × 648	15,000	0.767	11,498
704 × 520	20,000	0.782	15,631
640 × 640	17,500	0.798	13,970
640 × 512	21,000	0.832	17,463
640 × 376	30,000	0.793	23,780
512 × 512	25,000	0.873	21,829
512 × 320	42,000	0.832	34,926
512 × 264	50,000	0.847	42,335
512 × 224	60,000	0.832	49,895
320 × 264	75,000	0.903	67,737
320 × 192	100,000	0.931	93,138
256 × 256	87,500	0.998	87,317
256 × 144	150,000	1.035	155,230
256 × 128	162,750	1.073	174,634
256 × 64	300,000	1.164	349,269
128 × 128	262,500	1.331	349,269
128 × 64	420,000	1.663	698,538
128 × 48	525,000	1.774	931,384
128 × 24	775,000	2.404	1,862,769
128 × 16	775,000	3.605	2,794,154
64 × 16	775,000	7.211	5,588,309
64 × 8	775,000	14.421	11,176,618

Table B.2High-speed digital camera framerate and recording durations. Recording times (Rec. Times) are in seconds.

Figure B.1 High-speed digital camera. Shown with 60 mm lens.

Appendix C - Long-Distance Microscope and Lens Specifications

The Infinity K2 DistaMaxlong-distance microscope (LDM)attached to either the high-speed digital camera or the Particle Image Velocimetry (PIV) camera via a standard F-mount. Different close-focus (CF) lenses attached to the front of the LDM to achieve different levels of magnification.Table C.1provides the specifications of each of the CF attachments used with the LDM.

K2 DistaMax	STD			CF-1			CF-1/B			CF-2			CF-3			CF-4		
	Near	Mid	Far	Near	Mid	Far	Near	Mid	Far	Near	Mid	Far	Near	Mid	Far	Near	Mid	Far
WD mm	370	650	946	215	320	530	228	305	388	140	165	192	95	110	122	54	58	64
MAG	1.10	0.55	0.34	1.28	0.95	0.61	1.4	1.10	0.80	2.67	2.00	1.52	3.56	2.80	2.29	6.10	5.40	4.57
FOV mm	6.74	10	20.5	5.0	7.4	12.2	4.6	6.00	9.0	2.80	4.20	4.7	2.10	2.50	3.1	1.20	1.35	1.50

Table C.1Long-distance microscope lens working distance (WD), magnification (MAG), and field of view (FOV).

A Nikon AF Micro-Nikkor 60mm f/2.8D lens was also attached to either the high-speed camera or the PIV camera by a standard F-mount. The 60 mm lens had a minimum focus distance of 0.22 m. One or two 14 mm extension tubes (Nikon PK-12) were attached between the camera and the 60 mm lens to provide a small amount of magnification. Shown in Figure A.1.

Figure C.1 Long-distance microscope.

Appendix D - Software

High-Speed Video Capture and Processing

- Photron FASTCAM Viewer
- Version: 3.2.7

Particle Image Velocimetry Capture and Processing

- Insight 4G
- Version: 10.0.3.28

Vector Plots

- Tecplot Focus 2013 Release 1
- Build: 14.0.2.33360

Computational Fluid Dynamics

- ANSYS Fluent
- Version: 15.0.7

CFD Mesh Generation

- ANSYS ICEM CFD
- Version: 15.0.7

Appendix E - Auxiliary Instrumentation and Uncertainty Specifications

All measurements were gathered with the error relevant to each measurement device. The manufacturer-listed errors are summarized below. The test section inlet pressure was measured using a Viatran pressure transducer and calculated using both a liquid-filled pressure gauge and Bernoulli's principle. The test section outlet pressure was measured using an Omegadyne pressure transducer. The downstream reservoir (vacuum chamber) pressure was measured using the dry Ashcroft pressure gauge.

Pressure measurements

- Vacuum chamber:
    - Ashcroft dry pressure gauge (Figure E.1)
    - Range: -30-0 in Hg and 0-15 psig
    - Increment: 1 in Hg and 0.5 psig
    - Uncertainty: ± 2% of mid-scale (2.0 kPa)
- Test section inlet:
    - Viatran 245 (0-30 psia) pressure transducer: ± 0.1% FSO (0.21 kPa) (Figure E.3)
    - Wika liquid-filled pressure gauge (Figure E.1)
        - Range: -30-0 in Hg and 0-15 psig
        - Increment: 1 in Hg and 0.5 psig
        - Uncertainty: ± 1% mid-scale (1.0 kPa)
    - Test section inlet calculated and compared in two ways:
        - $P_{inlet} = (P_G + P_{atm}) - \rho g h_G$

- Where P_G was the gauge pressure measured at 2 Figure 2.1 and h_G was the height of the gauge below the test section inlet.
- Example for inlet pressure of 89.6 kPa shown in Figure 4.1:

$$P_{inlet} = \left((-3.4\ kPa) + 97.66\ kPa\right) - \left(998.2\ \frac{kg}{m^3}\right)\left(9.801\ \frac{m}{s^2}\right)(0.508\ m) = 89.3 \pm 1\ kPa$$

- $P_{inlet} = (P_{atm}) + \rho g h_T - \frac{\rho}{2} V_{inlet}^{\ 2}$
  - Where h_T was the height of the upstream reservoir (0.660 m for 104.0 kPa inlet pressure and -0.813 m for 89.6 kPa inlet pressure) above the test section inlet (negative if tank was below inlet elevation). V_{inlet} was the velocity at the test section inlet (~0.4 m/s at 30 ml/s).
  - Example for inlet pressure of 89.6 kPa shown in Figure 4.1:

$$P_{inlet} = (97.66\ kPa) + \left(998.2\ \frac{kg}{m^3}\right)\left(9.801\ \frac{m}{s^2}\right)(-0.813\ m) - \frac{\left(998.2\frac{kg}{m^3}\right)}{2}\left(0.4\ \frac{m}{s}\right)^2 = 89.6\ \pm 0.5\ kPa$$

- Test section outlet:
  - Omegadyne PX429-015A5V (0-15 psia) pressure transducer: ±0.08% BSL (0.083 kPa) (Figure E.3)
- Absolute pressure calibration:
  - A Princo barometer (Figure E.2) was used to calibrate and adjust all pressure measurements to absolute pressure. Barometer stated accuracy of 0.01 in Hg (0.034 kPa)

Figure E.1 Dry Ashcroft (left) and liquid-filled Wika (right) pressure gauges.

Flowrate measurements

- Fischer & Porter rotameter (Figure E.4):
    - 0.810 GPM at 1.0 S.G. max scale
    - 1% divisions
    - Uncertainly: ± 1% (0.51 ml/s)

Figure E.2 Barometer used for absolute pressure calibration, shown on side. Top of barometer shown in left side of photo.

Figure E.3Omegadyne (top) and Viatran (bottom) pressure transducers.

Figure E.4 Rotameter with attached liquid-filled pressure gauge.